Marine Strontium Isotope Evolution at the Triassic-Jurassic Transition Links Transient Changes in Continental Weathering to Volcanism of the Central Atlantic Magmatic Province

Bernát Heszler[1,2*], Joachim Katchinoff[3], László Palcsu[4], Anikó Horváth[4], Zsolt Vallner[1,5], Emma Blanka Kovács[1,6], Noah Planavsky[3], and József Pálfy[1,7]

[1]Department of Geology, Institute of Geography and Earth Sciences, Eötvös Lóránd University, Pázmány Péter sétány 1/C, Budapest H-1117, Hungary, [2]School of Earth Sciences, University of Bristol, Wills Memorial Building, Queens Road, Bristol BS8 1RJ, United Kingdom, [3]Department of Earth and Planetary Sciences, Yale University, New Haven, CT, 06511, USA, [4]Isotope Climatology and Environmental Research Centre (ICER), Institute for Nuclear Research, Debrecen H-4026, Hungary, [5]Department of Geology and Meteorology, University of Pécs, Ifjúság útja 6, Pécs H-7624, Hungary, [6]Department of Geology and Earth Surface Research Laboratory (ESRL), Trinity College Dublin, The University of Dublin, College Green, Dublin 2, Ireland, [7]HUN-REN–MTM–ELTE Research Group for Paleontology, Pázmány Péter sétány 1/C, Budapest H-1117, Hungary

[*]Corresponding author: Bernát Heszler (bernat.heszler@bristol.ac.uk)

Key Points:

- High-resolution $^{87}Sr/^{86}Sr$ data spanning 2.5 Myr across the end-Triassic extinction reveals multiphase perturbation of the marine Sr system
- Aggregation with other Sr data documents long-term and short-term changes over 8.5 Myr during the Triassic-Jurassic transition
- Modeling supports the role of volcanism of CAMP in a stepped weathering scenario of fresh basalt and continental crust

Abstract

The end-Triassic extinction (ETE) is one of the most severe biotic crises in the Phanerozoic. This event was synchronous with volcanism of the Central Atlantic Magmatic Province (CAMP), the ultimate cause of the extinction and related environmental perturbations. However, the continental weathering response to CAMP-induced warming remains poorly constrained. Strontium isotope stratigraphy is a powerful correlation tool that can also provide insights into the changes in weathering regime but the scarcity of $^{87}Sr/^{86}Sr$ data across the Triassic-Jurassic boundary (TJB) compromised the use of this method. Here we present new high-resolution $^{87}Sr/^{86}Sr$ data from bulk carbonates in Csővár, a continuous marine section that spans 2.5 Myrs across the TJB. We document a continuing decrease in $^{87}Sr/^{86}Sr$ the from the late Rhaetian to the ETE, terminated by a 300 kyr interval of no trend and followed by a transient increase in the early Hettangian that levels off. We suggest that the first in the series of perturbations is linked to the influx of non-radiogenic Sr from the weathering of freshly erupted CAMP basalts, leading to a delay in the radiogenic continental weathering response. The subsequent rise in $^{87}Sr/^{86}Sr$ after the TJB is explained by intensified continental crustal weathering from elevated CO_2 levels and reduced mantle-derived Sr flux. Using Sr flux modeling, we also find support for such multiphase, prolonged continental weathering scenario. Aggregating the new dataset with published records employing an astrochronological age model results in a highly resolved Sr isotope reference curve for an 8.5 Myr interval around the TJB.

Plain Language Summary

The end-Triassic mass extinction ~201 million years ago was one of the most severe crises in the history of life, triggered by massive volcanism in areas around the present-day Central Atlantic Ocean. Although volcanism is expected to produce greenhouse warming through carbon-dioxide outgassing that leads to increased weathering in the continents, finding direct proof for such a scenario is challenging. We report new measurements of ratios of strontium isotopes from marine limestones and reconstruct the weathering history at the Triassic-Jurassic transition. In the ocean, unradiogenic ^{86}Sr isotopes are sourced from submarine volcanism or weathering of fresh volcanic rocks from Earth's mantle, whereas radiogenic ^{87}Sr isotopes are delivered by rivers from weathering of rocks in Earth's continental crust. We find that a steady, long-term decreasing trend in strontium isotope ratio was disturbed by a series of short-term changes at the end of the Triassic. Supported by modeling, we suggest that these changes reflect the eruption of basalts of the Central Atlantic Magmatic Province and the effect of volcanism in intensifying the continental weathering. Knowing more detail about one component in a cascade of environmental changes ultimately helps our understanding of a critical event in the history of Earth and its biosphere.

1. Introduction

1.1. The End-Triassic Extinction Event and Global Change

The end-Triassic Extinction (ETE, 201.56 Ma (Blackburn et al., 2013)) is one of the major mass extinction events within the Phanerozoic, characterized by an ecosystem collapse that led to major turnovers in the biological systems in both marine and terrestrial groups (Marshall, 2023; Sepkoski Jr, 1996). This time interval around the Triassic-Jurassic boundary (TJB) is also characterized by severe perturbations of the ocean-atmosphere systems, such as global warming (McElwain et al., 1999), ocean acidification and decline in carbonate productivity (Greene et al., 2012), changes in sea level (Hallam & Wignall, 1999), and enhanced continental weathering (Cohen & Coe, 2007).

The end-Triassic extinction is also associated with disturbances in the global carbon cycle as evidenced by carbon isotope ($\delta^{13}C$) excursions (CIEs) observed in organic carbon and carbonate records (Hesselbo et al., 2002; Pálfy et al., 2001; Ward et al., 2001). Volcanism of the Central Atlantic Magmatic Province (CAMP) is increasingly accepted as the ultimate cause of the extinction and global environmental change (Pálfy & Kocsis, 2014), whereas the CAMP also initiated the breakup of the Pangea supercontinent and the opening of the Atlantic (McHone, 2000). Degassing likely triggered global warming (Capriolo et al., 2021) that promoted shallow marine anoxia (van de Schootbrugge & Wignall, 2015) and caused perturbations in the carbon cycle. Three successive negative carbon isotope excursions (NCIEs) related to the emplacement of the CAMP were identified and labelled as the “precursor” (P-NCIE), the “initial” (I-NCIE), and the “main” (M-NCIE) (Ruhl & Kürschner, 2011). The I-NCIE is associated with the main pulse of CAMP volcanism, and it is recognized in both marine and continental records (Deenen et al., 2010). These negative $\delta^{13}C$ anomalies are interpreted to reflect the sudden addition of

isotopically light carbon to the ocean-atmosphere system, possibly as CO_2 from volcanic degassing (Hesselbo et al., 2002), methane from thermal metamorphism of organic-rich sediments (Heimdal et al., 2020), biogenic methane from dissociation of gas hydrates (Pálfy et al., 2001), or some combination of these sources (Beerling & Berner, 2002; Hesselbo et al., 2007; Schaller et al., 2011).

Elevated Hg concentrations and Hg/TOC ratios in sections are among the best available proxies of coeval volcanism in both marine and terrestrial sedimentary successions and also helped to establish the connection between ETE and the emplacement of the CAMP (E. B. Kovács et al., 2020; Lindström et al., 2019; Percival et al., 2017; Ruhl et al., 2020; Shen et al., 2022a; Thibodeau et al., 2016; Yager et al., 2021). Two studies have reported a major $\delta^{238}U$ negative anomaly near the TJB, indicating the global spread of marine anoxia at and after the ETE (Jost et al., 2017; Somlyay et al., 2023). Positive $\delta^{34}S_{CAS}$ anomalies are also documented around the ETE, pointing to increased oceanic anoxia and pyrite burial for these intervals (He et al., 2020; Newton et al., 2004).

Although a growing body of paleontological, sedimentological, and geochemical evidence helps characterize the ETE and its connection to the volcanism of CAMP, not all feedback mechanisms of the Earth system at this event are fully resolved yet. A key aspect in understanding the global changes associated with the extinction event is the response of the weathering regime to the CO_2 outgassing from volcanism. Enhanced continental weathering is a potential mechanism linking volcanic activity and marine environmental perturbations, whereas chemical weathering of silicate rocks contributes to climate stabilization by the drawdown of atmospheric CO_2 (Berner et al., 1983). Local weathering proxies have been widely used for the ETE, such as clay mineralogy (Shen et al., 2022b; Zajzon et al., 2012), paleosols (van de

Schootbrugge et al., 2020), and the Os isotope systems (Cohen & Coe, 2007), and suggest abrupt changes in the weathering intensity in response to the emplacement of CAMP. However, temporally highly resolved, and accurate constraints on the weathering regime are still scarce for this time interval, partly due to the dearth of continuous marine sedimentary successions across the TJB.

1.2. The Latest Triassic-Earliest Jurassic Marine $^{87}Sr/^{86}Sr$ Record

Reconstruction of the $^{87}Sr/^{86}Sr$ evolution of ancient oceans can provide insights into weathering rates, global tectonic activity, and biogeochemical cycling throughout Earth's history (Chen et al., 2022; Elderfield, 1986; McArthur, 1994; Veizer & Compston, 1974). The strontium isotope composition of seawater has changed throughout geological history due to varying inputs from its two main sources (Burke et al., 1982). Hydrothermal influx from oceanic ridges and hotspots is relatively non-radiogenic with low $^{87}Sr/^{86}Sr$ ratio (~0.703), whereas more radiogenic strontium with high $^{87}Sr/^{86}Sr$ ratio (~0.714) is derived from the weathering of old continental crust and transported by rivers and groundwater (Elderfield, 1986; Jones & Jenkyns, 2001; McArthur, 1994; Pearce et al., 2015). Consequently, the $^{87}Sr/^{86}Sr$ ratio in seawater at any given time reflects the relative balance of inputs from continental and mantle reservoirs (Chen et al., 2022). The strontium isotopic composition of the ocean is homogenous due to its long residence time (~2.5 Myr) in comparison with the three magnitudes faster mixing time of the ocean (~1000 years) (Hodell et al., 1990), which enables the dating and global correlation of marine carbonates worldwide, through the development and use of a global $^{87}Sr/^{86}Sr$ reference curve (McArthur et al., 2020, and references therein).

Despite several studies investigating the long-term change of the $^{87}Sr/^{86}Sr$ ratio in Late Triassic-Early Jurassic records (Callegaro et al., 2012; Jones et al., 1994; Korte et al., 2003; Z.

Kovács et al., 2020; Onoue et al., 2022; Tackett et al., 2014), a reliable, continuous, and stratigraphically highly resolved and well-constrained dataset is still lacking across the TJB. The scarcity of such $^{87}Sr/^{86}Sr$ data hampers our understanding of the major environmental changes during this time interval. It remains controversial whether the emplacement of CAMP led to a significant change (or to any change) in the continuous long-term decrease of the $^{87}Sr/^{86}Sr$ ratio in the Late Triassic (Callegaro et al., 2012; Cohen & Coe, 2007; Jones et al., 1994; Korte et al., 2003; Z. Kovács et al., 2020; McArthur, 2008). Some records indicate for a brief reversal of this Late Triassic declining trend during the latest Rhaetian and earliest Hettangian, followed by a phase of negligible change, or even a transient increase, that persisted throughout the Hettangian stage (Callegaro et al., 2012; Cohen & Coe, 2007). This pattern, however, is not reflected in the global reference curve (McArthur, 1994; McArthur et al., 2012; McArthur et al., 2020) A LOESS statistical analysis of selected data implies a minor deceleration in the decline of marine $^{87}Sr/^{86}Sr$ ratio during the Hettangian (McArthur et al., 2020). However, there are no precise constraints for the magnitude or timing of this shift within the crucial time interval of the TJB due to the scarcity of reliable fossil skeletal materials (Korte et al., 2018; McArthur, 2008). The credibility of this interpretation also relies on the accuracy of the geological time scale, the correlation of sampling localities in Austria and the UK where $^{87}Sr/^{86}Sr$ data originated, as well as the preservation state of the samples (Hesselbo et al., 2002; Jones et al., 1994; Korte et al., 2003).

To resolve these issues, here we present the first high-resolution $^{87}Sr/^{86}Sr$ dataset across the TJB interval from a continuous marine section at Csővár in Hungary. We use the generated bulk carbonate Sr isotope data to assess the complex interplay between magmatic activity, weathering, and climate during the Triassic-Jurassic (T-J) transition. Furthermore, we develop an

astrochronological framework to enhance the correlation with other sections, then aggregate the previously published Sr isotope data for an improved global reference curve for strontium isotope stratigraphy (SIS) across this critical interval of Earth history. We employ modeling to reveal the most likely scenario of forcing the observed evolution of marine Sr isotope ratio and use it to reconstruct the changes in weathering regimes across the TJB.

2. Geological and Stratigraphic Setting

The Rhaetian to Hettangian Vár-hegy (Castle Hill) section near the village of Csővár in north-central Hungary, ~40 km northeast of Budapest (47°49′12.32″N 19°18′28.23″E, referred to as the Csővár section hereafter), is one of the rare continuous marine sections through the TJB globally (Pálfy & Dosztály, 2000). The outcrops of the area are situated within the fault-bounded Nézsa-Csővár block, which forms part of the Transdanubian Range Unit that, in turn, belongs to the ALCAPA Unit (or terrane) within the Alpine-Carpathian orogenic system (Haas & Tardy-Filácz, 2004). It represents the distal margin of the Dachstein Carbonate Platform along the western Neotethys shelf during the Late Triassic (Haas et al., 2010) (Figure 1). At this time, the shelf was divided by intra- and periplatform basins, such as the Csővár Basin, where the Csővár Formation was deposited. The formation consists of limestone deposited in slope, toe-of-slope and basinal environments (Haas et al., 1997).

The TJB at Csővár is recognised using biostratigraphy and carbon isotope chemostratigraphy. The fossil record of the Csővár section includes ammonoids, conodonts, radiolarians, foraminifera, and palynomorphs but is generally sparse. Nevertheless, a detailed biostratigraphical framework was developed that allows for constraining the TJB to a narrow stratigraphic interval (Götz et al., 2009; E. B. Kovács et al., 2020; Kozur, 1991, 1993; Pálfy et al., 2007; Pálfy et al., 2001; Pálfy & Dosztály, 2000). A distinctive negative carbon isotope

anomaly associated with the ETE was recorded from the Csővár section, recognized as one of the first NCIEs reported globally for the TJB (Pálfy et al., 2001). Subsequently, new high-resolution $\delta^{13}C_{carb}$ measurements on the Csővár section yielded a similar pattern (E. B. Kovács et al., 2020; Pálfy et al., 2007). The largest negative peak with an approximately -6‰ shift, observed between 17–18.4 m, is identified as the globally recognised I-NCIE. The P-NCIE and the extensive M-NCIE are not unambiguously evident in the Csővár record. In addition, a major mercury anomaly was detected, coincident with the I-NCIE, inferred to represent the onset of the extrusive phase of CAMP volcanism (E. B. Kovács et al., 2020). A negative shift in $\delta^{238}U$ between 17.6–21.6 meters is aligned with the I-NCIE and Hg anomalies, suggesting that globally significant seafloor anoxia also developed at the end of the Triassic and continued into the earliest Jurassic (Somlyay

et al., 2023).

The cyclostratigraphical analysis of elemental and stable isotope geochemical data from the Csővár section revealed periodicities comparable to the orbital cycles of the ~405 kyr long- and ~124 kyr short eccentricities, the ~34 kyr obliquity, and the ~17–21 kyr precession (Vallner et al., 2023). Thus, an astrochronological age model was developed for the approximately 52 m thick measured section, suggesting that it was deposited in 2.9–3 Myr, with an average sedimentation rate of 1.73–1.79 cm/kyr. Combining the cyclostratigraphy with previously published bio- and chemostratigraphical data allows a placement of the TJB at 21.8–22.2 m (i.e. Beds 58-59) (Vallner et al., 2023).

3. Materials and Methods

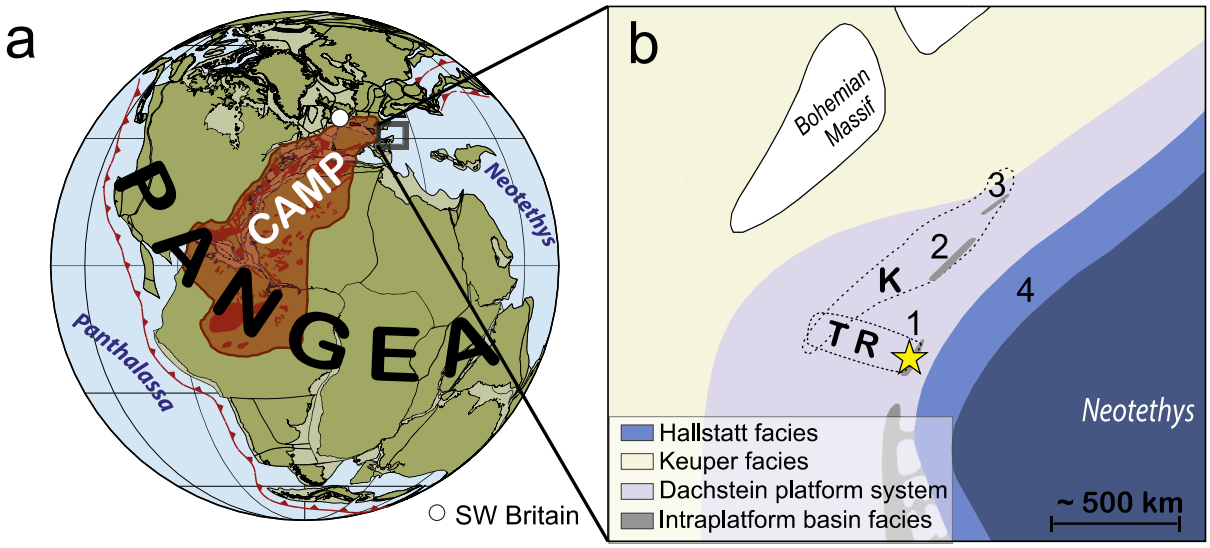

Figure 1. Late Triassic position of the Csővár section in a global (a) and regional (b) paleogeographical context. 1 – Csővár Basin, 2 – Eiberg Basin, 3 – Zliechov Basin, 4 – Zlambach section, TR – Transdanubian Range, K – Kössen-type basins. Modified after Haas & Tardy-Filácz , Rizzi et al. (2020) and Pálfy & Kocsis (2014).

3.1. Sampling and Preparation of Bulk Carbonate

Fine-grained, micritic bulk limestone rock samples were collected from the Csővár section and used for geochemical analyses. In total, seventy samples were chosen for $^{87}Sr/^{86}Sr$ isotope measurements and for elemental characterization. The sampled levels are identical to, but represent a selected subset of, those previously used to generate a high-resolution $\delta^{13}C_{carb}$ curve (E. B. Kovács et al., 2020) and carry out a cyclostratigraphical analysis (Vallner et al., 2023). The sample spacing is intentionally uneven, 20 cm around the ETE and TJB but less dense below and above. Any veins, stylolites, faults, and slumps were avoided during the sampling of the outcrop. Thin sections were prepared, and samples were selected for micro-drilling at Yale University after diagenetic screening based on petrographic observations, carefully avoiding any visible minor veins, surface weathering, and dolomite. Selected samples were micro-drilled with a tungsten-carbide bit to obtain powder for leaching.

3.2. Leaching of Samples

Strontium concentration in carbonate samples is generally low, making them sensitive to contamination from other phases during dissolution. This is particularly a concern for detrital silicate minerals, as they can introduce significant amounts of strontium into the sample, skewing the analytical results. Therefore, the samples were subjected to multi-step leaching procedures at the Yale Metal Geochemistry Center, Yale University, USA.

A pre-leach was applied, where samples were treated with 1 N ammonium acetate for a period of 30 minutes to remove loosely bound Rb and Sr cations. Samples were then centrifuged, with the supernatant being discarded and the solid powder being washed with ultrapure water (MQ2). This step was used to remove any sorption, exchangeable ions from the samples. After

the pre-leach, to target the calcite phase, while avoiding any dissolution of detrital phases, the samples were digested in dilute, 0.02 N HCl for 4 hours, then centrifuged and the supernatant collected. This was repeated for 2 hours, then for 10 minutes of digestion.

3.3. Major and Minor Element Analysis

The ratios of elements such as Li, Mg, Sr, Al, Mn, and Fe relative to Ca were determined using a Thermo Scientific Element XR ICP-MS (Inductively Coupled Plasma Mass Spectrometer) at the Yale Metal Geochemistry Center. The analysis was performed on a portion of the sample solutions that were first diluted with 5% HNO_3 and spiked with 1ppb of indium. Based on the measured Sr concentrations in the solutions, a specific amount of the aliquot was pipetted to achieve a target Sr concentration of 300 ppb.

3.4. Strontium Isotope Analysis

The column chromatography for the measurement of $^{87}Sr/^{86}Sr$ ratios was done in a Class 1000 cleanroom at the Isotope Climatology and Environmental Research Center at the Institute for Nuclear Research (ATOMKI) in Debrecen, Hungary. The samples were treated twice with 67% HNO_3 and dried, then dissolved in 4 x 1 ml 8 M HNO_3. For the column chemistry, crown-ether based Sr-Spec Resin (100–150 µm particle size) from Triskem International, France was used. Following the column chemistry, samples were treated with 2 x 1 ml 67% HNO_3, dried, and lastly each sample was dissolved in 1 ml 3% HNO_3 for strontium isotope analysis. Strontium isotope ratios ($^{87}Sr/^{86}Sr$) were measured on a Thermo Scientific NEPTUNE Plus multi-collector inductively coupled plasma mass spectrometer (MC-ICP-MS) equipped with an Aridus-3 (CETAC) desolvation system. Measured isotopic ratios for $^{87}Sr/^{86}Sr$ are corrected for instrumental mass discrimination using $^{88}Sr/^{86}Sr = 8.375209$, as well as by applying an

interference correction for $^{87}Rb^{+}$ and $^{86}Kr^{+}$ with $^{85}Rb^{+}$ and $^{83}Kr^{+}$, respectively. The measured ratios were calibrated against the standard NBS987 (NIST® SRM® 987) to the reported value of 0.710248 (McArthur et al., 2020). The uncertainties of the samples range between 0.000015 (0.0021%) and 0.000033 (0.0045%), with an average of 0.000017 (0.0025%) (±1σ). Nine standard NIST® SRM® 987 solutions that underwent column chemistry in the same manner as the limestone samples were analyzed and yielded a mean $^{87}Sr/^{86}Sr$ value of 0.710246 ± 0.000005 (±1σ), in good agreement with previous studies (McArthur et al., 2020, and references therein). Based on the results, the reproducibility was 0.000020 (±1σ), 28 ppm. Duplicate carbonate samples that went through the same leach process were within 0.005‰.

3.5. Stable Isotope Analysis

Thirty-one selected samples were run for carbon and oxygen isotopes at the Yale Analytical and Stable Isotope Center, using a KIEL IV Carbonate Device connected to a Thermo MAT 253 Isotope Ratio Mass Spectrometer. Carbon and oxygen isotopes aided in identifying the carbon isotope excursions associated with the TJB.

4. Results

4.1. Major and Minor Elements

The total of 70 samples were measured for major and minor elemental compositions. To accurately determine the most reliable $^{87}Sr/^{86}Sr$ ratios of pristine calcite, we used geochemical indicators, such as the Mn/Sr, Mn/Ca, Mg/Ca, Sr/Ca, and Rb/Sr ratios, to assess the detrital contribution and diagenetic alteration of carbonates. For the Mn/Sr ratio, the samples show an average of 0.17003, a minimum of 0.01287 and a maximum of 3.41425 (ppm/ppm). The Mn/Ca ratio has an average of 0.23928, with a minimum of 0.05 and a maximum of 1.4 (mmol/mol).

The Mg/Ca ratio has an average of 0.00602, with a minimum of 0.00238 and a maximum of 0.01147 (ppm/ppm). The Sr/Ca ratio yields an average of 2.12101, with a minimum of 0.24 and a maximum of 3.54 (mmol/mol). The detrital Rb/Sr ratio has an average of 0.00025, with a minimum of 0 and a maximum of 0.00296 (ppm/ppm).

4.2. Stable Isotopes

The newly obtained carbon isotope ($\delta^{13}C_{carb}$) values range from -3.6‰ to +3.32‰, with an average of -0.91‰ (Figure 2). Oxygen isotope ($\delta^{18}O$) data vary from -5.43‰ to -0.62‰, with an average of -2.23‰. The carbon isotope record is used to identify the major anomalies that are used for global correlation, primarily the I-NCIE. The carbon isotope trend of the new data is in good agreement with the results of previous stable isotope studies of the Csővár section (E. B. Kovács et al., 2020; Pálfy et al., 2007; Pálfy et al., 2001). From the base of the section, the first 10 m yield values around an average of 1.6‰. At 11 m there is an abrupt negative shift, reaching -0.15‰, the peak is followed by a 6 m gap in analyses, the trend then returns to more positive values. At 18 m, the most negative value of -3.51‰ is reached, followed by another negative peak of -3.17‰ at 21.65 m. After these major anomalies, there is a gradual return to more positive values, interrupted by a longer and more subtle negative shift reaching -0.1‰ at 25.7m. The oxygen isotope values show a similar trend, with an average of -1.4‰ for the first 10 m. A peak of -3.25‰ at 18 m and the most negative value of -3.59‰ at 21.65m. After the peak, the remainder of the section has an average value of -2.34‰.

4.3. Strontium Isotopes

The here generated $^{87}Sr/^{86}Sr$ ratios range from 0.70763 to 0.70895, with an average of 0.70772 (Figure 2), in broad agreement with previous Late Triassic–Early Jurassic SIS studies

(Korte et al., 2003; Z. Kovács et al., 2020; Onoue et al., 2022). The general trend of the profile from the base of the section is a continuous decrease in $^{87}Sr/^{86}Sr$ from 0.70773 to 0.70765 at 13 m, followed by a segment of no distinctive change up to 21.5 m, after which there is an increase in the $^{87}Sr/^{86}Sr$ to 0.70771 at 26.2 m and the values remain around 0.70769 up to the end of the section (Figure 2). These long-term subtle trends are interrupted by short-term positive $^{87}Sr/^{86}Sr$ anomalies. Three major positive anomalies are distinguished, the first one between 8.8 m to 12.4 m, reaching its peak at 10.2 m, 0.70773, the second one is between 16.9 m and 18.55 m, reaching 0.70769. The third one is between 21 m and 22 m, reaching 0.70771 at 21.2 m. A fourth minor, but distinguishable positive peak with small amplitude is observed at 26.2 m, reaching 0.70771.

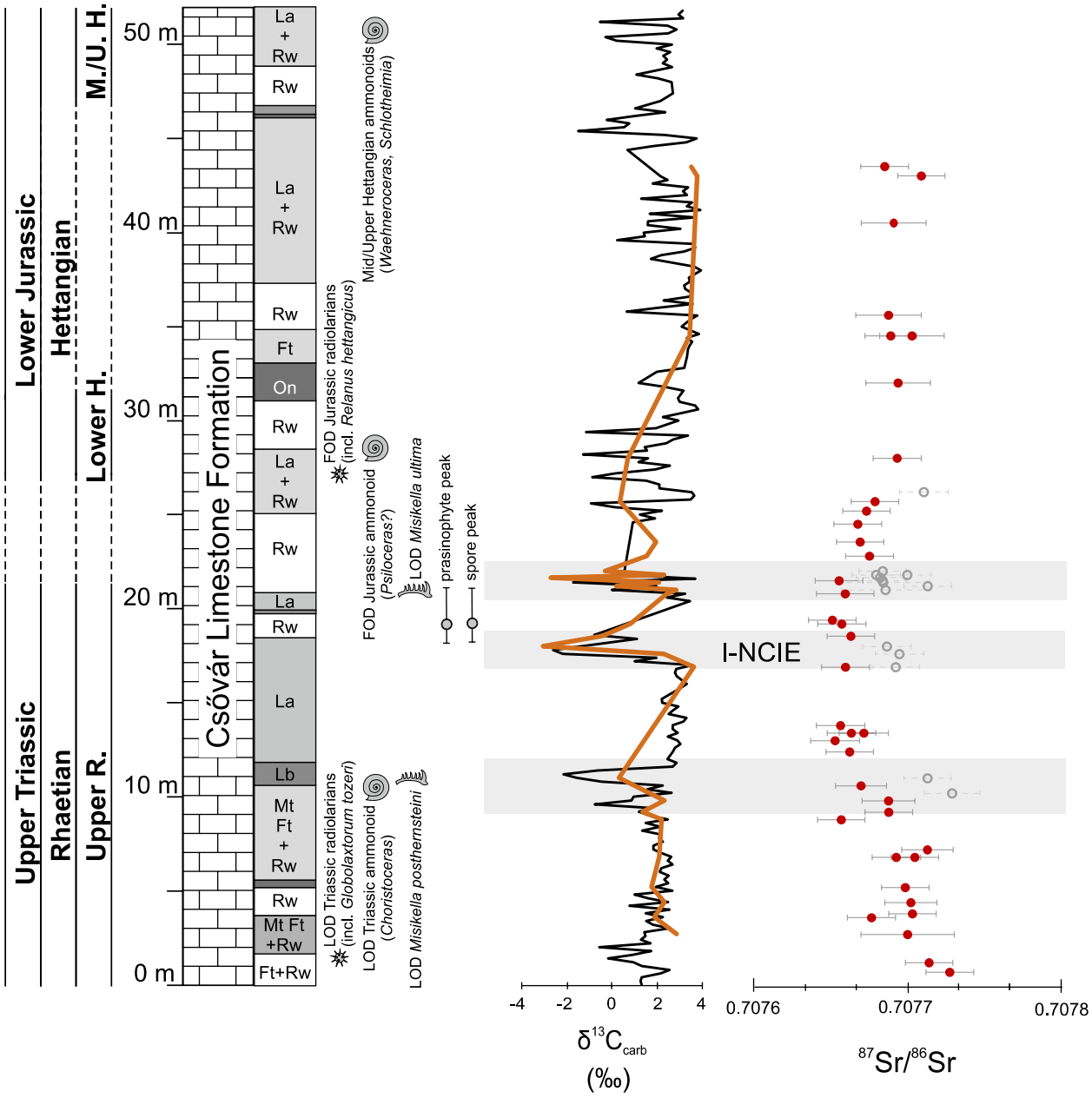

291

Figure 2. Strontium and carbon isotope data from the Csővár section and their litho-, bio-, and chronostratigraphic context. Carbon isotope curve from E. B. Kovács et al. (2020) (black line) and new data (orange line). Strontium isotope values marked by filled red circles and error bars are deemed reliable, those with open grey circles display a positive offset (see text for discussion). Grey shaded horizontal bars denote the most

prominent NCIEs that also correspond to levels with anomalously positive Sr ratios. Lithologic and microfacies log from Haas & Tardy-Filácz (2004) and E. B. Kovács et al. (2020). Rw: radiolarian wackestone, La: calcisiltite-calcilutite laminate, Ft: fine-grained turbidite, Mt: medium-grained turbidite, Lb: lithoclastic-bioclastic grainstone/packstone, On: oncoid, grapestone/packstone/ wackestone. Biostratigraphy from Pálfy & Dosztály (2000), Pálfy et al. (2001), Götz et al. (2009) and E. B. Kovács et al. (2020).

5. Discussion

5.1. Assessment of Possible Diagenetic Overprint

To faithfully reconstruct the $^{87}Sr/^{86}Sr$ ratio of ancient seawater, the analyzed material must be well-preserved. Although the results from bulk carbonates that are prone to subtle post-depositional alteration may be considered less reliable, they, nevertheless, can fall within the range of $^{87}Sr/^{86}Sr$ ratios measured in skeletal material of marine fossils. Geochemical screening and appropriate Sr extraction techniques increase the likelihood of obtaining marine signatures. Furthermore, in stratigraphic sequences where well-preserved fossils are scarce or non-existent, such as in the Precambrian or during mass extinction events such as the end-Permian or the ETE, the use of bulk carbonate rock remains the only practical method of continuous sampling for seawater $^{87}Sr/^{86}Sr$ studies (Chen et al., 2022; Halverson et al., 2007; Z. Kovács et al., 2020; Onoue et al., 2022; Saltzman & Sedlacek, 2013). The dissolution of bulk carbonate may lead to contamination of strontium from detrital aluminosilicate and diagenetic secondary phases, potentially resulting in inaccurate results, therefore proper diagenetic screening is needed (McArthur et al., 2020). Here, we evaluated the diagenetic alteration of every sample, and used only the results of the least altered ones in the reconstruction of $^{87}Sr/^{86}Sr$ trends.

The recent revision of Precambrian seawater $^{87}Sr/^{86}Sr$ curve, including new guidelines on different dissolution and diagenetic screening methods used in Sr isotopic work, provides the basis of our screening protocol for the bulk carbonate samples from the Csővár section (Chen et al., 2022). We used geochemical element ratios and cross-plot diagrams for assessing possible diagenetic processes that influenced the geochemical signal of the sedimentary sequence. Geochemical screening was carried out by using four elemental ratios, Mn/Sr, Mg/Ca, Sr/Ca, and Rb/Sr, combined with stable isotope data ($\delta^{13}C$, $\delta^{18}O$) and the assessment of $^{87}Sr/^{86}Sr$ ratios. The

Mn/Sr and Sr/Ca ratios are useful geochemical proxies to evaluate the preservation state of the samples, as both enrichment of Mn and depletion of Sr in a sample may indicate post-depositional alteration of the primary carbonate. Using the Mg/Ca ratio together with Mn/Sr and Sr/Ca ratios can help to identify modification of the primary carbonate during dolomitization. The Rb/Sr ratio is commonly used to evaluate the influence of terrigenous input on limestone samples. In general, diagenesis may lead to a decrease of Sr concentration in the samples, and alteration results in more radiogenic, higher $^{87}Sr/^{86}Sr$ ratios (Veizer & Compston, 1974). Therefore, significantly elevated $^{87}Sr/^{86}Sr$ ratios were considered altered. Specifically, we applied the following criteria to evaluate if the samples are well-preserved and represent the primary Sr signal:

$Mn/Sr < 0.1$ (Chen et al., 2022; Li et al., 2011; Zhou et al., 2020)

$Mg/Ca < 0.05$ (Chen et al., 2022; Li et al., 2011)

$Sr/Ca > 1$

$Rb/Sr < 0.04$ (Onoue et al., 2022; Onoue et al., 2018)

Additional sample screening was done using cross-plots (see Supporting Information Figure S1). Samples that did not meet the criteria were excluded from further analysis and interpretation. Overall, out of the 70 samples measured for Sr isotope stratigraphy, results of 52 samples were used in the interpretation (Figure 2).

5.2. The $\delta^{13}C_{carb}$ Record

The trend of the here reported $\delta^{13}C_{carb}$ data from the new suite of samples for Sr analysis agrees well with the values reported in previous studies of the Csővár section, in particular the more recent, higher resolution $\delta^{13}C_{carb}$ data (E. B. Kovács et al., 2020) (Figure 2). The $\delta^{13}C_{carb}$

curve displays major negative isotope anomalies that can be used for global chemostratigraphic correlations.

The carbon isotope trend of this study distinctly exhibits the I-NCIE, starting at 17.8 m, aligned closely with the pattern observed previously (E. B. Kovács et al., 2020). This concurrence underscores the reliability and consistency of the identified excursion and makes ground for its global correlation.

On the other hand, correlation of an earlier anomaly at ~11 m, previously tentatively suggested as the P-NCIE (E. B. Kovács et al., 2020), is revised here on the basis of cyclostratigraphy (Vallner et al., 2023). The time elapsed between this earlier anomaly and the onset of I-NCIE is 413 kyr which, compared to other sections and the duration of CAMP activity, is too long (Davies et al., 2017; Vallner et al., 2023) for an unambiguous correlation with the P-NCIE.

5.3. Characteristics of the High-Resolution $^{87}Sr/^{86}Sr$ curve

The $^{87}Sr/^{86}Sr$ profile of the Csővár section exhibit only gradual changes (Figure 2), which is typical of sedimentary sequences without stratigraphic gaps (Jones et al., 1994). The Sr isotope data, generated here for 2.5 Myr within the T-J transition (Vallner et al., 2023), records subtle shifts in the $^{87}Sr/^{86}Sr$ ratio that likely reflect the long-term global trend in the Sr isotope ratio. On the other hand, sudden changes, commonly less than 1 Myr in duration, may represent local changes in weathering or alteration of the original $^{87}Sr/^{86}Sr$ compositions (Richter & Turekian, 1993).

The $^{87}Sr/^{86}Sr$ record of the Csővár section displays three distinct short positive anomalies that coincide with NCIEs (Figure 2). The rate of change in these intervals is too high to reflect

359 solely global changes in the ocean system. Considering that the diagenesis screening did not
360 indicate alteration of these samples, this signal is inferred to reflect changes in the local
361 weathering regime.

362 In a comparable record, an abrupt shift to radiogenic $^{87}Sr/^{86}Sr$ values was reported from
363 the Fatra Formation in the Kardolína section (Onoue et al., 2022), which was located on the ramp
364 of the the southern margin of the Bohemian Massif in the NW Tethys region (Figure 1). The
365 Fatra Formation was deposited in a semi-restricted, shallow marine pull-apart basin, the Zliechov
366 Basin that was a part of the Austroalpine-West Carpathian shelf (Michalík et al., 2007). The
367 rapid shift in the $^{87}Sr/^{86}Sr$ ratio in the Kardolína section between the P-NCIE and I-NCIE is
368 interpreted as an increase in continental weathering in response to large-scale input of CO_2 from
369 CAMP activity, rather than global changes in seawater Sr isotope ratios (Onoue et al., 2022).

370 The amplitude of the positive $^{87}Sr/^{86}Sr$ shift in the Kardolína section is more than five
371 times greater than that of the Csővár section, which can be accounted for by the differences in
372 depositional settings at the two sites. The Rhaetian Fatra Formation was deposited on the
373 southern edge of the Bohemian Massif and reflects the increased weathering of the hinterland
374 dominated by Variscan granitoids. The Csővár basin, on the other hand, was an intraplatform
375 basin close to the distal margin of the Dachstein platform and farther from continental influence,
376 which may explain why the short-term positive $^{87}Sr/^{86}Sr$ shifts are more subdued. The
377 coincidence of these short-term shifts in the Sr isotope signal with N-CIEs suggests that CAMP-
378 induced transient pulses of local weathering intensity are correlated with carbon cycle
379 perturbations. However, to understand the long-term global changes occurring during the ETE
380 interval and the T-J transition as a response to CAMP activity, elevated atmospheric CO_2 levels,

and variations in continental weathering, only the screened $^{87}Sr/^{86}Sr$ values (excluding the positive anomalies) from the Csővár section are used (Figure 2).

The base of the Csővár section yields values starting from ~0.70773, which is in accordance with the extension of the persistent unradiogenic trend from the Late Norian (Z. Kovács et al., 2020; McArthur et al., 2020). The decreasing trend to ~0.70765 continues up to 13 m, followed by a leveling at values between ~0.70765-0.70766 up to ~21 m. This flat interval with no trend is characterized by the most unradiogenic values in the section and is attributed to a large mantle-derived Sr flux to the oceans, related to the early phase of CAMP activity (Heimdal et al., 2020). The flat segment transitions into an increasing trend between ~21 m and ~26 m toward a more radiogenic value of ~0.70769, which remains relatively constant for the remainder of the section. The start of the increasing trend in the $^{87}Sr/^{86}Sr$ ratios postdates the I-NCIE and could be caused by the continental weathering increase in response to elevated atmospheric CO_2 levels triggered by the emplacement of CAMP. The complex, multiphase evolution of the Sr isotope curve in the Csővár section reveals multiple shifts in the balance of unradiogenic and radiogenic Sr fluxes, correlation with the onset of CAMP volcanism and the I-NCIE, and changes in continental weathering intensity and changes in exposed areas of fresh basalts.

5.4. Integrating the $^{87}Sr/^{86}Sr$ Record with Other Geochemical Proxies

The newly obtained data is consistent with previous geochemical studies conducted in the Csővár section and expands our knowledge about the events and feedback mechanisms during the ETE. Major mercury anomalies coincident with the I-NCIE, with Hg concentrations peaks at 18.8 m (668 ppb) and 19.4 m (972 ppb), were interpreted to reflect the onset of the extrusive phase of CAMP volcanism (E. B. Kovács et al., 2020) (Figure 3). Additional but less pronounced

Hg peaks were also observed in the Hettangian part of the Csővár section, which are likely associated with later pulses of CAMP activity. Notably, however, no Hg enrichment was

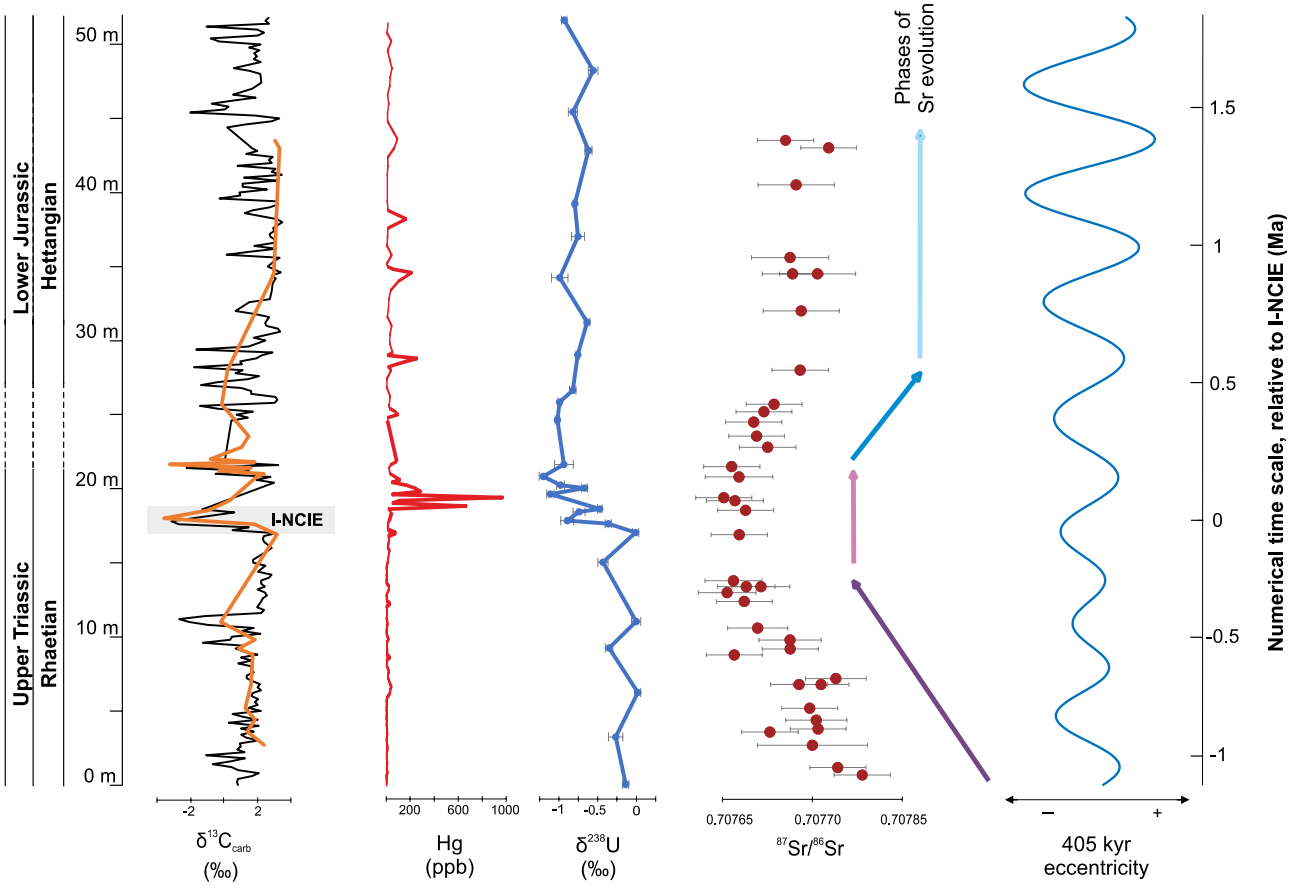

Figure 3. Multiproxy geochemical records of the Csővár section. $\delta^{13}C$ from E. B. Kovács et al. (2020) in black, and this study, in orange. Hg concentrations from E. B. Kovács et al. (2020), $\delta^{238}U$ from Somlyay et al. (2023), $^{87}Sr/^{86}Sr$ this study. Filtered long eccentricity cycles and numerical time scale from Vallner et al. (2023).

observed before the I-NCIE. Similarly, the $\delta^{238}U$ values display a relatively high average of -0.22‰, with no major shift before the I-NCIE (Somlyay et al., 2023) (Figure 3). A substantial drop in $\delta^{238}U$ to -0.93‰ at 17.6 m indicates a major and abrupt increase in the global extent of

bottom-water anoxia. The onset of this negative shift in the uranium isotope ratios corresponds with the I-NCIE at 17.8 m and indicates a link between the carbon cycle perturbation and marine anoxia with the CAMP volcanism as their possible common cause (Somlyay et al., 2023). The protracted excursion of uranium isotopes suggests that there were sustained oxygen-depleted conditions globally even after the TJB. Coincidently, the more radiogenic $^{87}Sr/^{86}Sr$ trend after the event is congruent with this observation, which is likely the result of enhanced weathering intensity, consequently lead to elevated nutrient delivery, therefore higher primary productivity rates. Additionally, the influx of less dense freshwater may have facilitated the development of water column stratification that, together with the elevated seawater temperatures, could cause a decline in oxygen solubility and inefficient ventilation, ultimately leading to the formation and persistence of anoxic bottom conditions (Jost et al., 2017; Somlyay et al., 2023).

In contrast, the changes in the $^{87}Sr/^{86}Sr$ ratio in the section appear to commence before the I-NCIE. The leveling off in the $^{87}Sr/^{86}Sr$ ratio begins at ~13 m, predating the onset of the eruptive activity of CAMP as recorded by the Hg spike. Intrusion of dike and sill systems could have resulted in the release of massive amounts of isotopically light carbon as thermogenic methane from subsurface organic-rich strata (Heimdal et al., 2020; Ruhl & Kürschner, 2011). The resultant increase in atmospheric greenhouse gas concentration is expected drive intensified weathering. However, the $^{87}Sr/^{86}Sr$ record from Csővár does not show any shift to radiogenic values before the TJB, only a leveling off of the $^{87}Sr/^{86}Sr$ curve. Possibly, any increase in continentally derived radiogenic Sr was compensated by the unradiogenic Sr input from weathering of newly erupted CAMP basalts, resulting in a relatively stable, dynamically balanced seawater $^{87}Sr/^{86}Sr$ ratio. Following the I-NCIE and TJB, there is a delayed turn towards radiogenic trend in the $^{87}Sr/^{86}Sr$ ratio, which then levels off again and persists up to the end of

the section, i.e. middle/late Hettangian. The rise in radiogenic Sr was delayed due to direct unradiogenic influx and weathering of CAMP, which initially counterbalanced the influx of continental crustal Sr. Ultimately, prolonged weathering of continental crust outpaced the unradiogenic Sr input from the rapid weathering of CAMP-derived basalts (Cohen & Coe, 2007), which led to a delayed but pronounced rise in radiogenic Sr in the system. This suggests that prolonged weathering played a crucial role in regulating the geochemical response of the Earth system to CAMP activity.

5.5. Astrochronological Framework and Correlation of Sections Sourcing Sr data

Major challenges in reconstructing the changes in marine $^{87}Sr/^{86}Sr$ ratios through the T-J transition stem from correlation ambiguities and lack of precise age control in sections that yielded the isotope data. To resolve these issues, here we attempt to incorporate the new Csővár record into a global dataset of $^{87}Sr/^{86}Sr$ ratios reported in earlier publications. To develop a highly resolved reference curve for the T-J transition, we use a robust astrochronological framework of overlapping sections correlated by selected chemo- and biostratigraphic tie points.

The recently developed cyclostratigraphy for the Csővár section (Vallner et al., 2023) is useful for correlation with other TJB sections. Cyclostratigraphy of several representative sections in the Northern Calcareous were used to constrain the Late Triassic numeric time scale (Galbrun et al., 2020), while strontium isotope analyses were carried out in the same set of sections (Z. Kovács et al., 2020). Combining data from these two studies, we attempt to provide numerical age constraints for the samples analysed for $^{87}Sr/^{86}Sr$ by Z. Kovács et al. (2020) to allow their direct comparison with the new data from the Csővár section.

We argue that the approach of a cyclostratigraphic analysis of a Rhaetian composite record assembled from four overlapping Austrian reference sections (Steinbergkogel, Zlambach,

Eiberg, and Kuhjoch) (Galbrun et al., 2020) is fraught with problems caused by different lithologies. Instead, we re-analysed the individual sections for cyclostratigraphy separately here, based on the magnetic susceptibility variations reported in Galbrun et al. (2020). We also re-assessed the correlation of sections that was originally established on their bio- and lithostratigraphy (Galbrun et al., 2020). We focus on those sections that have a well-established and biostratigraphically constrained carbon isotope record such as the Eiberg and Zlambach sections. Although the cyclostratigraphic analysis of the Kuhjoch section, that serves as the Hettangian GSSP (Hillebrandt et al., 2013), was also attempted, it proved unsuitable to assign astrochronological ages to the samples with Sr data (Z. Kovács et al., 2020) for poor preservation of cyclicity. The Eiberg and Zlambach sections were correlated based on biostratigraphy (Galbrun et al., 2020), as the boundary of the Rhaetian *Vandaites stuerzenbaumi* and *Choristoceras marshi* zones is well-defined in both sections. The correlation between the Eiberg and Kuhjoch sections is based on the presence of a dark, organic-rich regional marker bed marking the top of the Kössen Formation, referred to as the "T-bed", located at the top of the Eiberg section and near the base of the Kuhjoch section. In these two sections, the T-bed is characterized by a rapid increase in magnetic susceptibility intensity and a marked negative carbon isotope shift, identified as the I-NCIE. Thus, the Alpine sections can be correlated to the Csővár section via the I-NCIE. The numerical age of the I-NCIE is set to 201.56 (Blackburn et al., 2013; Davies et al., 2017), providing an anchor for the floating astrochronologies. The age of the TJB, based on the first occurrence of the ammonoid *Psiloceras spelae tirolicum* (Hillebrandt et al., 2013) is 201.36 ± 0.17 Ma (Wotzlaw et al., 2014). The $^{87}Sr/^{86}Sr$ ratios determined from the Alpine sections are characterized by considerable scatter but overall, their trend aligns well with the long-term Late Triassic decline (Z. Kovács et al., 2020) (Figure 4).

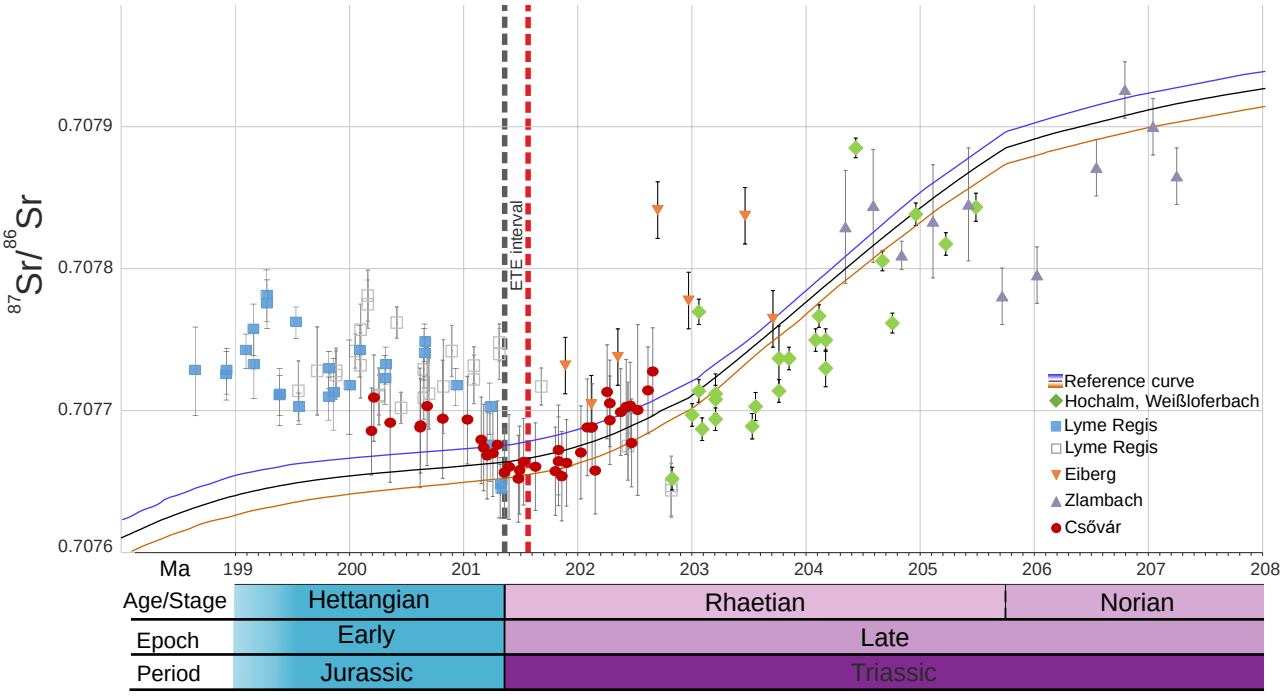

Figure 4. Compilation of selected $^{87}Sr/^{86}Sr$ data from the TJB interval and their comparison with the reference curve in GTS 2020 (McArthur et al., 2020). Error bars are 2sd. Diamonds: Hochalm, Weißloferbach brachiopods (Korte et al., 2003), squares: Lyme Regis oysters (Jones et al., 1994), orange triangles: bulk carbonate from Eiberg, purple triangles: bulk carbonate from Zlambach (the Northern Calcareous Alps) (Z. Kovács et al., 2020), circles: bulk carbonate from Csővár (this study). Red dashed line represents the I-NCIE at 201.56 Ma (Davies et al., 2017), black dashed line represents the TJB at 201.36 Ma. Ages are plotted using floating astrochronological age models (see text) or recalculated to the GTS 2020 (Gradstein et al., 2020). From Lyme Regis, age of solid squares is based on recalculation, that of open squares are astrochonologically calibrated after Weedon et al. (2018).

Although the Kuhjoch section could not be confidently astronomically calibrated, its Sr data warrant discussion nonetheless. Samples in close proximity to the T-bed (within 30 cm) have high values (~0.7078) (Z. Kovács et al., 2020). At similar stratigraphic position around the I-NCIE in the Csővár section, samples yield lower values at ~0.70765. Because secondary alteration commonly leads to an increase in Sr isotope ratios, the lower values from Csővár are considered more reliable, also suggested by their better alignment with the global $^{87}Sr/^{86}Sr$ trend. As for the lowermost Hettangian, two samples from Kuhjoch show high values of 0.70784 and 0.70780, which are higher than any other Hettangian data (Jones et al., 1994; Z. Kovács et al., 2020). This questions the reliability of the samples from Kuhjoch and stresses the importance of new data from the Hettangian.

An extensive Early Jurassic $^{87}Sr/^{86}Sr$ dataset for the Hettangian was generated using mainly oyster shells from Lyme Regis, Dorset (UK) (Jones et al., 1994). The original ages assigned by Jones et al. (1994) were distributed among numerical tie-points using the assumption of equal durations for ammonite subzones, but this method must be approached with caution (McArthur, 2008; Pálfy & Dosztály, 2000). Moreover, three samples formerly regarded as Rhaetian (H7, H12, H22) originate from strata in the lower Blue Lias, which is now considered Hettangian (Weedon et al., 2018). Because of uncertainties regarding the numerical ages of Jones et al. (1994), we not only recalculated their ages according to the Geologic Time Scale 2020 (GTS 2020) (Gradstein et al., 2020) but also employed an alternative approach, using the cyclostratigraphic and biostratigraphic age model of Weedon et al. (2019) to establish numerical ages for the $^{87}Sr/^{86}Sr$ ratios of Lyme Regis. The I-NCIE has not been identified at Lyme Regis (Korte et al., 2009), therefore the age of the first known bed from the Tilmanni Zone (H6) is set to 201.36 Ma, i.e. approximated using the age of the TJB (Hillebrandt et al., 2013; Wotzlaw et

al., 2014). However, a controversy surrounds the duration of ~ 4.1 Myr for the Hettangian proposed from a combined analysis of sections in SW England (Weedon et al., 2019), as such long stage duration is at odds with several other studies (Hüsing et al., 2014; Ruhl et al., 2010; Storm et al., 2020), including that from the Csővár section (Vallner et al., 2023). Derived exclusively from the Lyme Regis section, the Hettangian is still suggested to span ~ 3 Myr, a duration that remains longer than suggested by others (Weedon et al., 2019).

5.6. Integration of the $^{87}Sr/^{86}Sr$ Record with Global Data for an Improved Reference Curve

To maximize the usefulness of the new results reported here, the Csővár record is aggregated with and compared to published $^{87}Sr/^{86}Sr$ data from England (Jones et al., 1994) and the Northern Calcareous Alps in Austria (Korte et al., 2003; Z. Kovács et al., 2020), both for an improved reference curve and for insights into the drivers of the observed changes. In addition, we also present a comparison with the latest reference curve in the GTS 2020 (McArthur et al., 2020) (Figure 4). Following the opinion of McArthur et al. (2020), no conodont data is used in this compilation, due to their sensitivity to alteration after burial, commonly resulting in significant offset of their $^{87}Sr/^{86}Sr$ values. The Rhaetian brachiopod data of Korte et al. (2003) are included with numerical ages recalculated using the GTS 2020. The Hettangian data from oyster samples (Jones et al., 1994) were excluded from GTS 2020, due to their assumed secondary alteration (McArthur, 2008). However, we suggest that they record primary seawater signatures, based on the close fit with the data from Csővár, in addition to the geochemical indicators of well-preserved skeletal calcite (Jones et al., 1994). However, we recalculated their age to the GTS 2020 (from Jones et al., 1994). We also present this $^{87}Sr/^{86}Sr$ dataset (Jones et al., 1994) along the numerical age model from cyclostratigraphy of the Dorset coast section

(Weedon et al., 2018). The $^{87}Sr/^{86}Sr$ values from the Northern Calcareous Alps (Z. Kovács et al., 2020) and the Csővár section are also astronomically calibrated and correlated using the I-NCIE, numerically calibrated at 201.564 Ma (Blackburn et al., 2013; Davies et al., 2017). To focus on the long-term global changes, the values corresponding to the short-term and presumably local positive $^{87}Sr/^{86}Sr$ anomalies (see section 5.3.) are omitted from the Csővár dataset. Thus, the Sr isotope data from Csővár spanning ~2.5 Myr, is substantially expanded by the compiled dataset, covering ~8.5 Myr across the T-J transition (Figure 4).

The compiled dataset displays a continuous decrease from the Late Triassic until the ETE interval. This trend starts in the Norian, as revealed by the brachiopod samples of Korte et al. (2003). Bulk carbonate data provide a wider context but show some scatter, especially from the Eiberg section, nevertheless also support the overall decrease in the Late Triassic (Z. Kovács et al., 2020). The Eiberg section consists of mixed siliciclastics and carbonates deposited in an intraplatform basin. There is less scatter in the data from the Zlambach section that exposes a sequence deposited on a toe-of-slope to open marine basinal environment between the Dachstein platform and the Hallstatt basin.

The long-term decreasing trend continues with the Csővár record that fits well with the data from the Northern Calcareous Alps (Korte et al., 2003; Z. Kovács et al., 2020). The decline of the $^{87}Sr/^{86}Sr$ ratio terminates at the ETE and gives way to a short flat segment with no significant change for ~300 kyr. This trough at the ETE interval is followed by an increasing trend in the earliest Hettangian. The Csővár data thus connects the decreasing Rhaetian values from the Alps to the increasing Hettangian trend observed in England. Notably, in both the Csővár and the Dorset records the rising limb gives way to another, protracted nearly flat

546 segment up to the Middle-Late Hettangian, supporting the case that the samples of Jones et al.
547 (1994) indeed reflect the original seawater Sr signal.

548 The pattern of the Csővár $^{87}Sr/^{86}Sr$ ratios suggests the injection of significant amounts of
549 unradiogenic Sr into seawater due to the emplacement of CAMP and weathering of basalt during
550 the ETE interval. However, such direct impact of CAMP on marine $^{87}Sr/^{86}Sr$ appears
551 counterbalanced by related other changes in the Earth surface system. Ultimately, enhanced
552 hydrological cycling and increased continental weathering of more radiogenic continental rocks
553 due to elevated CO_2 could have contributed to the delivery of relatively radiogenic Sr to the
554 global ocean with higher $^{87}Sr/^{86}Sr$ ratios, first cancelling out the decrease, then resulting in a
555 Hettangian rise in seawater $^{87}Sr/^{86}Sr$ (Cohen & Coe, 2007).

556 In a global context, the average values of the Csővár data yield relatively low $^{87}Sr/^{86}Sr$
557 values of only limited scatter that aligns well with the general trend of previously published data,
558 indicating that well-preserved bulk carbonate samples yield reliable results. The characteristic
559 pattern serves as a basis for interpretation and validation of modeling results. Previously, the
560 scarcity of reliable data from the TJB interval severely limited the applicability of SIS. The
561 inclusion of results from the Csővár section significantly extends and enhances the robustness of
562 the global $^{87}Sr/^{86}Sr$ dataset, by filling a gap in the T-J transition interval and revealing a rise in
563 the marine $^{87}Sr/^{86}Sr$ ratio after the TJB, following the Late Triassic long-term decrease and a
564 temporary flattening of the curve. Although the oyster data of Lyme Regis (Jones et al., 1994) is
565 in good agreement with the Sr isotope ratios presented here, more data is needed to confirm the
566 $^{87}Sr/^{86}Sr$ trend of the Hettangian. An unresolved issue is to constrain the start of the return of the
567 long-term declining trend in the Sinemurian (Jones & Jenkyns, 2001), which may be connected
568 with the opening of the Central Atlantic ocean basin (Marzoli et al., 2018). The decreasing trend

569 is terminated by a rebound to more radiogenic values only near the Pliensbachian-Toarcian
570 boundary, with a low $^{87}Sr/^{86}Sr$ ratio close to 0.7070 at the next inflection point of the curve
571 (McArthur et al., 2000), which is likely related to the emplacement of the Karoo-Ferrar large
572 igneous province, marking another event of global significance.

573 **5.7. Modeling Sr Flux Perturbations around the TJB**

574 We use strontium isotope mass balance box modeling to explore the cycling of strontium
575 among the Earth's oceanic, crustal, and mantle reservoirs and can thus provide additional insights
576 into the observational record. By incorporating knowledge of strontium isotope ratios, fluxes,
577 and reservoirs, models can reproduce changes in seawater composition and therefore help in
578 identifying the underlying mechanisms that influenced the strontium cycle during the TJB
579 interval. Here, we use a simple forward box model to estimate the impact of perturbations on the
580 ocean Sr cycle that could explain the changes in seawater $^{87}Sr/^{86}Sr$ ratio observed during the TJB
581 interval. Thereby, we examine how continental weathering and hydrothermal inputs of Sr may
582 have responded to extensive large igneous province (LIP) volcanism. Here, the hydrothermal
583 input is understood as the sum of all mantle-derived Sr input and is not restricted to Sr input from
584 MORB-related hydrothermal sources. We employ a model developed by Yobo et al. (2021),
585 where a coupled Sr mass and Sr-isotope mass balance approach was used. The model parameters
586 are derived from modern values but are adapted to the end-Triassic (Table 1). The following
587 Equation (1) was employed to compute changes in the oceanic Sr inventory over time:

588 $$\frac{dN^{Sr}}{dt} = F_{riv} + F_H + F_{dia} - F_{ppt} \qquad (1)$$

589 where N^{Sr} represents the number of moles of strontium present in the oceans, and the variables
590 correspond to the fluxes of strontium, which include riverine sources (continental weathering,

591 F_{riv}), hydrothermal sources (F_H), diagenetic sources (F_{dia}), and carbonate precipitation flux (F_{ppt}),

592 respectively. Changes in ocean $^{87}Sr/^{86}Sr$ over time were calculated using Equation (2):

593 $$\frac{dR_{SW}^{Sr}}{dt} = \frac{F_{riv}^{Sr}(R_{riv}^{Sr} - R_{SW}^{Sr}) + F_H^{Sr}(R_H^{Sr} - R_{SW}^{Sr}) + F_{dia}^{Sr}(R_{dia}^{Sr} - R_{SW}^{Sr})}{N_{Sr}} \quad (2)$$

594 where R_{SW}^{Sr} represents the $^{87}Sr/^{86}Sr$ ratio of the oceanic Sr reservoir, influenced by the $^{87}Sr/^{86}Sr$

595 ratios of Sr inputs from riverine (R_{riv}^{Sr}), hydrothermal (R_H^{Sr}), and diagenetic (R_{dia}^{Sr}) sources,

596 respectively.

597 The Sr input fluxes and their $^{87}Sr/^{86}Sr$ ratios were obtained from present-day estimates

598 and adjusted to end-Triassic values whenever possible and justified (Table 1). The model was

599 run for 3 million years, which is in broad agreement with the time of deposition the studied

600 section at Csővár (Vallner et al., 2023)

601 The initial Sr isotope mass balance is normalized to the end-Triassic contemporaneous

602 seawater isotope value (~0.70773) (Figure 5). Therefore, the initial $^{87}Sr/^{86}Sr$ ratio of all

603 continental weathering sources of Sr (F_{riv}) is adjusted from 0.71040 (present-day ratio) to 0.7086

604 to achieve a steady state $^{87}Sr/^{86}Sr$ ratio of ~0.70773 for end-Triassic seawater based on values

Table 1. Parametrization of the Sr box model. Strontium fluxes and isotopic estimates adapted from Yobo et al. (2021) and references therein.

Symbol	Description	Modern Value	Model Value	Source
F_{riv}^{Sr}	Continental weathering flux	66.1 x 10^9 mol yr^{-1}	66.1 x 10^9 mol yr^{-1}	1
R_{riv}^{Sr}	Continental weathering isotopic composition	0.7104	0.7101	2
F_{HT}^{Sr}	Hydrothermal flux	8.4 x 10^9 mol yr^{-1}	14.1 x 10^9 mol yr^{-1}	1
R_{HT}^{Sr}	Hydrothermal isotopic composition	0.7035	0.7035	1
F_{dia}^{Sr}	Diagenetic flux	5.5 x 10^9 mol yr^{-1}	5.5 x 10^9 mol yr^{-1}	1
R_{dia}^{Sr}	Diagenetic isotopic composition	0.70849	0.70733	3
N^{Sr}	Amount of Sr in seawater	1.25 x 10^{17} mol	1.25 x 10^{17} mol	4

1. Peucker-Ehrenbrink & Fiske (2019)
2. Allègre et al. (2010)
3. Li & Elderfield (2013)
4. Palmer & Edmond (1989)

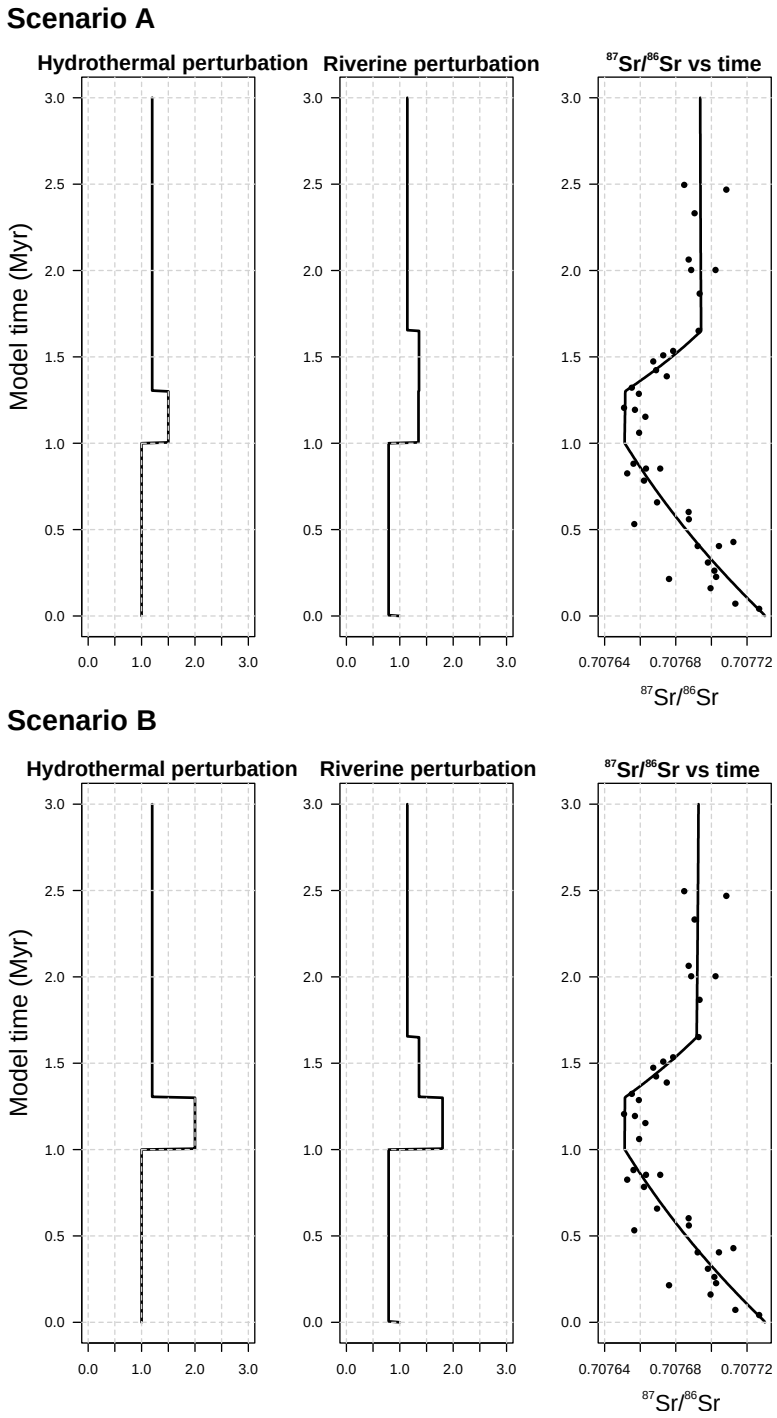

Figure 5. Box model simulations of perturbations in both the hydrothermal and riverine Sr fluxes required to reproduce the change in seawater $^{87}Sr/^{86}Sr$ ratios during the T-J transition observed in the Csővár section. The emplacement of CAMP and the contemporaneous carbon isotope excursion (I-NCIE) begin at 1 Myr model time, with

perturbations normalized to the assumed steady state at model time 0 Myr. Scenario A: Hydrothermal flux increased by 1.5x at the onset of LIP eruptions. The hydrothermal flux falls back to 1.2x from 1.3 Myr model time but remains elevated throughout. To achieve the decreasing trend till 1 Myr, the riverine flux is reduced to 0.79x. The riverine flux in response to the onset of CAMP increases to 1.35x and remains elevated till 1.65 Myr, resulting in a radiogenic trend that is then reduced to 1.14x and remains elevated until the end of the model. Scenario B: Hydrothermal flux increased by 2x at the onset of LIP eruptions, then falls back to 1.2x from 1.3 Myr. To balance the high hydrothermal flux, the riverine perturbation increases to 1.8x in response to CAMP and recovers stepwise to 1.36x at 1.3 Myr and 1.14x at 1.65 Myr. In both scenarios, the hydrothermal and weathering fluxes remain elevated, reflecting the ongoing volcanism of CAMP and incipient opening of the Atlantic in the earliest Jurassic.

obtained from the base of the Csővár section. This adjustment may not reflect the true value of the continental weathering regime, it only serves as an initial value that makes comparison possible with the assumed steady state baseline conditions. The primary input fluxes of Sr to the oceans, F_{riv} and F_H, drive changes in the oceanic Sr cycle (Allègre et al., 2010; Elderfield, 1986; Li & Elderfield, 2013; Peucker-Ehrenbrink & Fiske, 2019). Modifying either one or both fluxes induce changes in the $^{87}Sr/^{86}Sr$ ratio of seawater, which would then gradually approach a new steady state $^{87}Sr/^{86}Sr$ ratio and slows down exponentially with time. In order to accurately simulate past changes, incorporating geological constraints is essential for implementing the box model and achieving the most realistic scenario. This way, previous studies, models, and proxy data were considered when modeling the changes in Sr fluxes to the ocean (Z. Kovács et al.,

615 2020; Yobo et al., 2021). These model scenarios reflect the change in Sr flux with respect to the
616 presumed initial state, and they attempt reproduce the stepwise nature of change and the
617 protracted rise in the $^{87}Sr/^{86}Sr$ ratio.

618 From multiple model-runs with different setups, two of the resulting scenarios best
619 replicated our observational data (Figure 5), (i) the mantle-derived flux set to 1.5x (Scenario A)
620 or (ii) the mantle-derived flux set to 2x (Scenario B), compared to the assumed initial steady
621 state and in response to CAMP volcanism. The decreasing trend in the $^{87}Sr/^{86}Sr$ ratio is
622 reproduced by reducing the weathering rates compared to the initial steady state. This
623 assumption is supported by multiple pieces of evidence for early onset of hydrothermal activity
624 in the Late Triassic (Callegaro et al., 2012; Z. Kovács et al., 2020). The $^{87}Sr/^{86}Sr$ ratio remains
625 around its nadir in response to the onset of the extrusive phase of the CAMP volcanism for ~300
626 kyr, then increases towards more radiogenic values. This rise in $^{87}Sr/^{86}Sr$ ratios observed during
627 the TJB interval may have been caused by either (i) the intensification in continental crustal
628 weathering (Cohen & Coe, 2007; Shen et al., 2022b) in response to the elevated atmospheric
629 CO_2 concentrations (Schaller et al., 2011), or (ii) a rapid decrease in mantle-derived Sr flux.
630 However, the eruptions of large volumes of equatorial CAMP basalts ($^{87}Sr/^{86}Sr$ ~ 0.7035-0.7050
631 (Heimdal et al., 2019; Merle et al., 2011)) would have intensified volcanic weathering as well,
632 forcing the oceanic $^{87}Sr/^{86}Sr$ ratio towards unradiogenic values. Furthermore, the erosion and
633 intense weathering of the CAMP basalts started immediately after their emplacement (Cohen &
634 Coe, 2002, 2007), which aligns with the fluctuations in atmospheric CO_2 levels responding to the
635 episodic volcanic and/or thermogenic CO_2 release (Schaller et al., 2011). We suggest the ~300
636 kyr stable low $^{87}Sr/^{86}Sr$ ratios were caused by the excess unradiogenic Sr from weathered fresh
637 basalts at the start of the extrusive phase of CAMP volcanism counteracting the increasing

638 contribution from enhanced continental crustal weathering. The duration of this interval is
639 probably tied to CAMP emplacement, but likely also reflects the weathering history of the basalt.
640 Although CAMP volcanism resulted in the subaerial emplacement of massive amounts of basalt,
641 thick soil cover would have developed in regions of lower elevation, decreasing the weathering
642 rates. Our multiphase prolonged weathering scenario is supported by the measured $^{87}Sr/^{86}Sr$
643 ratios from Csővár and the Sr flux modeling across the TJB interval. Scenario B (with a twofold
644 increase in the mantle-derived Sr and the intensified continental weathering) provides the best
645 model-data fit. Schaller et al. (2011) argued for a doubling of atmospheric pCO_2 in response to
646 the first CAMP pulse, followed by a decrease to pre-eruption concentrations over ~300 kyr.
647 After the first peak of pCO_2, there was a decline to below background levels, which can be
648 attributed to the prompt consumption of CO_2 resulting from an overall increase in continental
649 weathering (Schaller et al., 2012). The here proposed scenario (Scenario B, Figure 5) for the Sr
650 isotopic signal is also consistent with $^{187}Os/^{188}Os$ changes across the TJB (Figure 6), related to
651 the release of significant amounts of unradiogenic Os into the global ocean from the weathering
652 of young mantle-derived basalts (Cohen & Coe, 2002, 2007; Kuroda et al., 2010). This pattern
653 agrees well with the occurrence of the minimum and inflections in the marine $^{87}Sr/^{86}Sr$ record, as
654 both can be linked to the emplacement and immediate weathering of the flood basalt province.
655 We find that the $^{87}Sr/^{86}Sr$ ratio remained consistently low immediately following the
656 initial CAMP eruptions for ~300 kyr, suggesting an unradiogenic ^{86}Sr dominated weathering flux
657 in the global oceanic Sr budget. As the highly weatherable CAMP basalts were largely
658 consumed, or developed a thick soil cover (Cohen & Coe, 2002, 2007; Marzoli et al., 2018), the
659 proportion of unradiogenic components progressively decreased, explaining the delayed onset
660 and protracted increase in $^{87}Sr/^{86}Sr$ ratio.

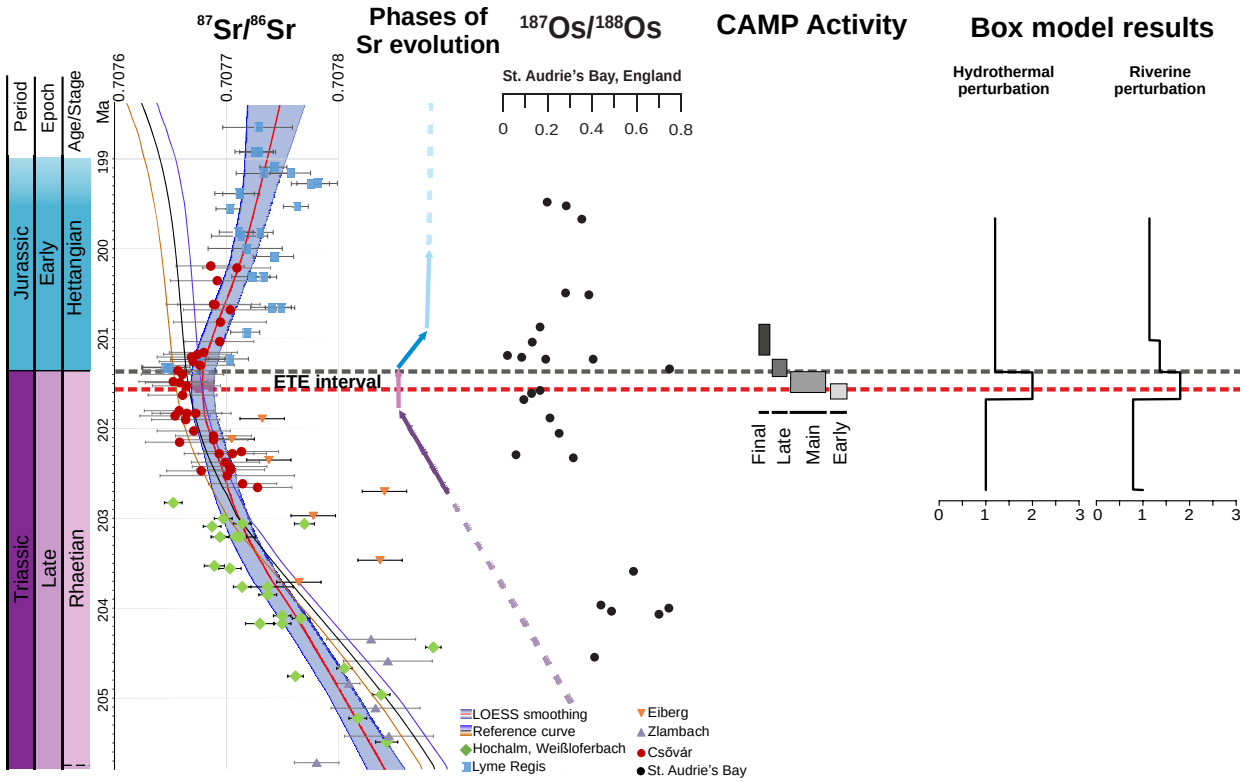

Figure 6. Comparison of a new LOESS smoothed curve (f=0.5) of the compiled $^{87}Sr/^{86}Sr$ dataset and the reference curve of McArthur et al. (2020) for the TJB interval. List all the localities with their references. The osmium isotope data is from Cohen & Coe (2002). The age distribution of CAMP basalts (extrusive phases) is from Heimdal et al. (2020). Box model output (twofold hydrothermal perturbation) is from this study (Scenario B).

5.8. Comparison with the Sr Isotope Record of Other LIP-driven Global Events

Similar to the end-Triassic extinction (ETE), associated with the CAMP volcanism, other LIPs have been also identified as possible drivers of environmental, climatic, and biotic changes throughout Earth history (Bond & Grasby, 2017; Wignall, 2005). As the control of various LIP

665 emplacements on the marine $^{87}Sr/^{86}Sr$ ratios is still debated (Ingram & DePaolo, 2022), a brief
666 comparison of our end-Triassic case study and other analogous events is warranted.
667 The emplacement of the Siberian Traps is considered to be the ultimate driver of the end-
668 Permian extinction, the most severe mass extinction in the Phanerozoic (Benton & Twitchett,
669 2003; Dal Corso et al., 2022). The global oceanic Sr isotopic signal increased continuously from
670 the Paleozoic minimum value (include value here and reference) in the Middle Permian
671 (Capitanian) to the Early Triassic (Korte & Ullmann, 2018; McArthur et al., 2020).
672 Contradictorily, both a short-term acceleration (Song et al., 2015) and deceleration (Korte &
673 Ullmann, 2018) in the rate of $^{87}Sr/^{86}Sr$ ratio increase have been previously proposed to reflect the
674 Siberian Traps LIP emplacement and the associated changes in weathering rates. However, the
675 roles of riverine Sr flux (more radiogenic values) and fresh basalts weathering (more
676 unradiogenic isotopic composition) received different emphases (Korte & Ullmann, 2018; Song
677 et al., 2015). As our study questions the validity of conodont Sr isotope data, we regard the
678 brachiopod-based data and proposed acceleration (Korte & Ullmann, 2018) to be more likely
679 than the conodont-based measurements and suggested deceleration (Song et al., 2015). Although
680 the long-term trends in the Late Permian and Late Triassic are opposing, a stepwise short-term
681 response in the Sr system to the emplacement and weathering of continental flood basalts and
682 climatically enhanced weathering of the continental crust occurs at both the EPE and ETE.
683 Following the CAMP, the Karoo-Ferrar LIP was emplaced in the Early Jurassic,
684 coinciding with a second-order extinction event and perturbations in the marine biogeochemical
685 cycles (Jenkyns, 2010; Pálfy & Smith, 2000). A Sr isotope profile is established at very high
686 resolution and integrated with ammonite biostratigraphy in Yorkshire, England (McArthur et al.,
687 2000). The long-term decline in $^{87}Sr/^{86}Sr$ is terminated at a clear inflection point near the

Pliensbachian-Toarcian boundary and followed by a steep rise in the Early Toarcian (Jones et al., 1994), coincident with the Jenkyns Event (or Toarcian Oceanic Anoxic Event, T-OAE). Thus, this hyperthermal event, triggered by the Karoo-Ferrar LIP volcanism, is expressed in a climate-driven increase in radiogenic continental weathering flux.

The Cretaceous is punctuated by several Oceanic Anoxic Events (OAEs) that are also associated with LIP volcanism and show distinctive $^{87}Sr/^{86}Sr$ signatures (Ingram & DePaolo, 2022; Jenkyns, 2010). The characteristic response at major Cretaceous OAEs is observed as pronounced negative $^{87}Sr/^{86}Sr$ excursions. The declines in the $^{87}Sr/^{86}Sr$ during both the Early Aptian OAE 1a (or Selli Event) (Jones & Jenkyns, 2001) and the Cenomanian-Turonian OAE 2 (or Bonarelli Event) (Yobo et al., 2021), were likely driven by the sudden increase in mantle-sourced submarine volcanism, as both events are synchronous with the genesis of oceanic plateau basalts.

As demonstrated above, the geochemical response to LIP-associated global events is not uniform. The changes in the global $^{87}Sr/^{86}Sr$ ratio associated with LIP-driven events are the result of complex processes, with each case exhibiting unique characteristics. First-order differences exist between continental and submarine LIP emplacement on the $^{87}Sr/^{86}Sr$ ratio. The balance is also affected by ongoing system-wide changes in the background, such as long-term climate change and orogenic activity, which can influence the weathering rates, erosion patterns, and sediment transport, affecting the marine Sr isotopic composition. Therefore, a case-by-case approach is needed for understanding the specific factors at play in each LIP event and their relative influence on the global oceanic $^{87}Sr/^{86}Sr$ ratio. In the T-J transition, the CAMP-induced changes as revealed in this study provide an example for continental flood basalts emplaced at low latitudes. In this case, at hundred-thousands-year scale first the transient effect of weathering

711 of freshly erupted lava is predominant, before the protracted, climatically driven increase in
712 continental crustal weathering becomes more significant in influencing the global $^{87}Sr/^{86}Sr$ ratio.

713 **6. Conclusions**

714 Here, we present the first high-resolution $^{87}Sr/^{86}Sr$ dataset across the TJB interval from
715 the biostratigraphically and chemostratigraphically well-constrained continuous marine TJB
716 section at Csővár, to resolve uncertainties about the timing and magnitude of change in the
717 mantle-derived and continental weathering fluxes of Sr to the global ocean. Based on the 52
718 well-preserved samples that represent a 2.5-Myr depositional history, anchored to carbon isotope
719 stratigraphy and cyclostratigraphy, the $^{87}Sr/^{86}Sr$ ratio displays modest but distinctive variations:
720 (i) the steady but gentle latest Triassic decline is terminated by (ii) a near stagnant, low isotopic
721 ratio near the system boundary (near the initial NCIE), followed by (iii) an increase in the
722 $^{87}Sr/^{86}Sr$ ratio in the earliest Jurassic, then a (iv) leveling off in the values.

723 The Sr data from Csővár is aggregated with published data from the Northern Calcareous
724 Alps and SW England that are also astrochronologically dated and correlated using integrated
725 carbon isotope stratigraphy and biostratigraphy. The composite dataset spans 8.5 Myr across the
726 T-J transition. From the late Norian, it displays a long-term decrease that is followed by a
727 complex, multiphase perturbation starting near the ETE, a 300-kyr-interval of stagnant, low
728 isotopic ratio and a subsequent rise in the marine $^{87}Sr/^{86}Sr$ ratio before achieving a new steady-
729 state in the Hettangian. This suggests that the influx of unradiogenic Sr into coeval seawater
730 from the weathering of fresh CAMP basalt delayed the prolonged continental crustal weathering
731 response, caused by elevated atmospheric CO_2 levels, supplying radiogenic Sr to the global
732 ocean and increasing the $^{87}Sr/^{86}Sr$ ratios.

We can reproduce the $^{87}Sr/^{86}Sr$ results using a forward mass balance model output with forcing from early hydrothermal activity in the latest Triassic, followed by emplacement and weathering of freshly erupted basalts that transiently withheld the development of a radiogenic trend. A radiogenic Sr pulse only commenced after the peak eruptive phase of CAMP and after large volumes of CAMP had been rapidly eroded.

The new $^{87}Sr/^{86}Sr$ data from Csővár, incorporated into a larger dataset, as well as forward box model simulations of the Sr flux, point towards a complex, multiphase scenario of enhanced continental weathering during the TJB interval. Our results increase the resolution and the correlation power of Sr isotope stratigraphy across the T-J transition. However, further Sr isotope studies are needed from other marine successions in this interval, with a similar level of detail to validate the proposed mechanisms for the changes in the global Sr isotopic signal. The comparison of our results with other global events of LIP-related environmental and biotic perturbations highlights that, although enhanced weathering is a common element of the cascade of environmental effects, each event may be unique and different in their detailed history as recorded in the Sr isotope evolution.

Acknowledgments

We are grateful to John McArthur for sharing the LOESS 6 look-up table. We thank Eric Bellefroid and Joshua West for help in field sample collecting. Brad Erkkila assisted in the C and O isotope analysis. Lucien Nana Yobo generously shared the R code used for modeling. We benefited from helpful discussions with Zsófia Kovács, Tamás Müller and Anna Somlyay. János Haas and Clemens Ullmann offered useful comments on a thesis that formed the basis of this manuscript. NJP acknowledges support from the Packard Foundation. Funding from NKFIH OTKA Grant K135309 is acknowledged. The research was partly supported by the European

Union and the State of Hungary, co-financed by the European Regional Development Fund in the project of GINOP-2.3.2.-15-2016-00009 ‘ICER’. This is HUN-REN–MTM–ELTE Paleo contribution No. 3XY.

Conflict of Interest

The authors declare no conflicts of interest relevant to this study.

Data Availability Statement

All geochemical, elemental composition and isotope data, together with box-model R code are presented as Supporting Information. The supplementary materials are archived at Zenodo (https://zenodo.org/) under https://doi.org/10.5281/zenodo.10522076.

References

Allègre, C. J., Louvat, P., Gaillardet, J., Meynadier, L., Rad, S., & Capmas, F. (2010). The fundamental role of island arc weathering in the oceanic Sr isotope budget. *Earth and Planetary Science Letters*, 292(1-2), 51-56. https://doi.org/10.1016/j.epsl.2010.01.019

Beerling, D., & Berner, R. (2002). Biogeochemical constraints on the Triassic-Jurassic boundary carbon cycle event. *Global Biogeochemical Cycles, 16*(3), 10-11-10-13. https://doi.org/10.1029/2001GB001637

Benton, M. J., & Twitchett, R. J. (2003). How to kill (almost) all life: the end-Permian extinction event. *Trends in Ecology & Evolution, 18*(7), 358-365. https://www.sciencedirect.com/science/article/pii/S0169534703000934

Berner, R. A., Lasaga, A. C., & Garrels, R. M. (1983). The carbonate-silicate geochemical cycle and its effect on atmospheric carbon-dioxide over the past 100 million years. *American Journal of Science, 283*(7), 641-683. https://doi.org/10.2475/ajs.283.7.641

Blackburn, T. J., Olsen, P. E., Bowring, S. A., McLean, N. M., Kent, D. V., Puffer, J., et al. (2013). Zircon U-Pb geochronology links the end-Triassic extinction with the Central Atlantic Magmatic Province. *Science, 340*(6135), 941-945. https://doi.org/10.1126/science.1234204

Bond, D. P. G., & Grasby, S. E. (2017). On the causes of mass extinctions. *Palaeogeography, Palaeoclimatology, Palaeoecology, 478*, 3-29. https://doi.org/10.1016/j.palaeo.2016.11.005

Burke, W., Denison, R., Hetherington, E., Koepnick, R., Nelson, H., & Otto, J. (1982). Variation of seawater $^{87}Sr/^{86}Sr$ throughout Phanerozoic time. *Geology, 10*(10), 516-519. https://doi.org/10.1130/0091-7613(1982)10<516:VOSSTP>2.0.CO;2

Callegaro, S., Rigo, M., Chiaradia, M., & Marzoli, A. (2012). Latest Triassic marine Sr isotopic variations, possible causes and implications. *Terra Nova, 24*(2), 130-135. https://doi.org/10.1111/j.1365-3121.2011.01046.x

Capriolo, M., Mills, B. J. W., Newton, R. J., Corso, J. D., Dunhill, A. M., Wignall, P. B., & Marzoli, A. (2021). Anthropogenic-scale CO_2 degassing from the Central Atlantic Magmatic Province as a driver of the end-Triassic mass extinction. *Global and Planetary Change*, 103731. https://doi.org/10.1016/j.gloplacha.2021.103731

Chen, X., Zhou, Y., & Shields, G. A. (2022). Progress towards an improved Precambrian seawater $^{87}Sr/^{86}Sr$ curve. *Earth-Science Reviews, 224*, 103869. https://doi.org/10.1016/j.earscirev.2021.103869

798 Cohen, A. S., & Coe, A. L. (2002). New geochemical evidence for the onset of volcanism in the
799 Central Atlantic magmatic province and environmental change at the Triassic-Jurassic
800 boundary. *Geology*, *30*(3), 267-270. https://doi.org/10.1130/0091-
801 7613(2002)030<0267:NGEFTO>2.0.CO;2
802 Cohen, A. S., & Coe, A. L. (2007). The impact of the Central Atlantic Magmatic Province on
803 climate and on the Sr-and Os-isotope evolution of seawater. *Palaeogeography,*
804 *Palaeoclimatology, Palaeoecology*, *244*(1-4), 374-390.
805 https://doi.org/10.1016/j.palaeo.2006.06.036
806 Dal Corso, J., Song, H., Callegaro, S., Chu, D., Sun, Y., Hilton, J., et al. (2022). Environmental
807 crises at the Permian–Triassic mass extinction. *Nature Reviews Earth & Environment*,
808 *3*(3), 197-214. https://doi.org/10.1038/s43017-021-00259-4
809 Davies, J., Marzoli, A., Bertrand, H., Youbi, N., Ernesto, M., & Schaltegger, U. (2017). End-
810 Triassic mass extinction started by intrusive CAMP activity. *Nature Communications*,
811 *8*(1), 15596. https://doi.org/10.1038/ncomms15596
812 Deenen, M. H., Ruhl, M., Bonis, N. R., Krijgsman, W., Kuerschner, W. M., Reitsma, M., & Van
813 Bergen, M. (2010). A new chronology for the end-Triassic mass extinction. *Earth and*
814 *Planetary Science Letters*, *291*(1-4), 113-125. https://doi.org/10.1016/j.epsl.2010.01.003
815 Elderfield, H. (1986). Strontium isotope stratigraphy. *Palaeogeography, Palaeoclimatology,*
816 *Palaeoecology*, *57*(1), 71-90. https://doi.org/10.1016/0031-0182(86)90007-6
817 Galbrun, B., Boulila, S., Krystyn, L., Richoz, S., Gardin, S., Bartolini, A., & Maslo, M. (2020). "
818 Short" or" long" Rhaetian? Astronomical calibration of Austrian key sections. *Global and*
819 *Planetary Change*, *192*, 103253. https://doi.org/10.1016/j.gloplacha.2020.103253

Götz, A., Ruckwied, K., Pálfy, J., & Haas, J. (2009). Palynological evidence of synchronous changes within the terrestrial and marine realm at the Triassic/Jurassic boundary (Csővár section, Hungary). *Review of Palaeobotany and Palynology, 156*(3-4), 401-409. https://doi.org/10.1016/j.revpalbo.2009.04.002

Gradstein, F. M., Ogg, J. G., Schmitz, M. D., & Ogg, G. M. (2020). *Geologic Time Scale 2020*: Elsevier.

Greene, S. E., Martindale, R. C., Ritterbush, K. A., Bottjer, D. J., Corsetti, F. A., & Berelson, W. M. (2012). Recognising ocean acidification in deep time: An evaluation of the evidence for acidification across the Triassic-Jurassic boundary. *Earth-Science Reviews, 113*(1-2), 72-93. https://doi.org/10.1016/j.earscirev.2012.03.009

Haas, J., Götz, A. E., & Pálfy, J. (2010). Late Triassic to Early Jurassic palaeogeography and eustatic history in the NW Tethyan realm: New insights from sedimentary and organic facies of the Csővár Basin (Hungary). *Palaeogeography, Palaeoclimatology, Palaeoecology, 291*(3-4), 456-468. https://doi.org/10.1016/j.palaeo.2010.03.014

Haas, J., Tardi-Filácz, E., Oravecz-Scheffer, A., Góczán, F., & Dosztály, L. (1997). Stratigraphy and sedimentology of an Upper Triassic toe-of-slope and basin succession at Csővár, North Hungary. *Acta Geologica Hungarica, 40*(2), 111-177.

Haas, J., & Tardy-Filácz, E. (2004). Facies changes in the Triassic–Jurassic boundary interval in an intraplatform basin succession at Csővár (Transdanubian Range, Hungary). *Sedimentary Geology, 168*(1-2), 19-48. https://doi.org/10.1016/j.sedgeo.2004.03.002

Hallam, A., & Wignall, P. B. (1999). Mass extinctions and sea-level changes. *Earth-Science Reviews, 48*, 217–250. https://doi.org/10.1016/S0012-8252(99)00055-0

Halverson, G. P., Dudás, F. Ö., Maloof, A. C., & Bowring, S. A. (2007). Evolution of the $^{87}Sr/^{86}Sr$ composition of Neoproterozoic seawater. *Palaeogeography, Palaeoclimatology, Palaeoecology, 256*(3-4), 103-129. https://doi.org/10.1016/j.palaeo.2007.02.028

He, T., Dal Corso, J., Newton, R. J., Wignall, P. B., Mills, B. J., Todaro, S., et al. (2020). An enormous sulfur isotope excursion indicates marine anoxia during the end-Triassic mass extinction. *Science advances, 6*(37), eabb6704. https://doi.org/10.1126/sciadv.abb6704

Heimdal, T. H., Callegaro, S., Svensen, H. H., Jones, M. T., Pereira, E., & Planke, S. (2019). Evidence for magma–evaporite interactions during the emplacement of the Central Atlantic Magmatic Province (CAMP) in Brazil. *Earth and Planetary Science Letters, 506*, 476-492. https://doi.org/10.1016/j.epsl.2018.11.018

Heimdal, T. H., Jones, M. T., & Svensen, H. H. (2020). Thermogenic carbon release from the Central Atlantic magmatic province caused major end-Triassic carbon cycle perturbations. *Proceedings of the National Academy of Sciences, 117*(22), 11968-11974. https://doi.org/10.1073/pnas.2000095117

Hesselbo, S. P., McRoberts, C. A., & Pálfy, J. (2007). Triassic–Jurassic boundary events: Problems, progress, possibilities. *Palaeogeography, Palaeoclimatology, Palaeoecology, 244*(1-4), 1-10. https://doi.org/10.1016/j.palaeo.2006.06.020

Hesselbo, S. P., Robinson, S. A., Surlyk, F., & Piasecki, S. (2002). Terrestrial and marine extinction at the Triassic-Jurassic boundary synchronized with major carbon-cycle perturbation: A link to initiation of massive volcanism? *Geology, 30*(3), 251-254. https://doi.org/10.1130/0091-7613(2002)030<0251:TAMEAT>2.0.CO;2

Heszler, B. (2024). Marine Strontium Isotope Evolution at the Triassic-Jurassic Transition Links

Transient Changes in Continental Weathering to Volcanism of the Central Atlantic Magmatic Province [Data set]. Zenodo. https://doi.org/10.5281/zenodo.10522076

Hillebrandt, A., Krystyn, L., Kürschner, W., Bonis, N., Ruhl, M., Richoz, S., et al. (2013). The global stratotype sections and point (GSSP) for the base of the Jurassic System at Kuhjoch (Karwendel Mountains, Northern Calcareous Alps, Tyrol, Austria). *Episodes, 36*(3), 162-198. https://doi.org/10.18814/epiiugs/2013/v36i3/001

Hodell, D. A., Mead, G. A., & Mueller, P. A. (1990). Variation in the strontium isotopic composition of seawater (8 Ma to present): Implications for chemical weathering rates and dissolved fluxes to the oceans. *Chemical Geology: Isotope Geoscience section, 80*(4), 291-307. https://doi.org/10.1016/0168-9622(90)90011-Z

Hüsing, S., Beniest, A., van der Boon, A., Abels, H., Deenen, M., Ruhl, M., & Krijgsman, W. (2014). Astronomically-calibrated magnetostratigraphy of the Lower Jurassic marine successions at St. Audrie's Bay and East Quantoxhead (Hettangian–Sinemurian; Somerset, UK). *Palaeogeography, Palaeoclimatology, Palaeoecology, 403*, 43-56. https://doi.org/10.1016/j.palaeo.2014.03.022

Ingram, B. L., & DePaolo, D. J. (2022). Sr Isotopes in Seawater: Stratigraphy, Paleo-tectonics, Paleoclimate, and Paleoceanography. *Elements in Geochemical Tracers in Earth System Science*. https://doi.org/10.1017/9781108991674

Jenkyns, H. C. (2010). Geochemistry of oceanic anoxic events. *Geochemistry Geophysics Geosystems, 11*, Q03004. https://doi.org/10.1029/2009GC002788

Jones, C. E., & Jenkyns, H. C. (2001). Seawater strontium isotopes, oceanic anoxic events, and seafloor hydrothermal activity in the Jurassic and Cretaceous. *American Journal of Science, 301*(2), 112-149. https://doi.org/10.2475/ajs.301.2.112

887 Jones, C. E., Jenkyns, H. C., & Hesselbo, S. P. (1994). Strontium isotopes in Early Jurassic
888 seawater. *Geochimica et Cosmochimica Acta, 58,* 1285-1301.
889 https://doi.org/10.1016/0016-7037(94)90382-4
890 Jost, A. B., Bachan, A., van De Schootbrugge, B., Lau, K. V., Weaver, K. L., Maher, K., &
891 Payne, J. L. (2017). Uranium isotope evidence for an expansion of marine anoxia during
892 the end-T riassic extinction. *Geochemistry, Geophysics, Geosystems, 18*(8), 3093-3108.
893 https://doi.org/10.1002/2017GC006941
894 Korte, C., Hesselbo, S. P., Jenkyns, H. C., Rickaby, R. E., & Spötl, C. (2009).
895 Palaeoenvironmental significance of carbon-and oxygen-isotope stratigraphy of marine
896 Triassic–Jurassic boundary sections in SW Britain. *Journal of the Geological Society,*
897 *166*(3), 431-445. https://doi.org/10.1144/0016-76492007-177
898 Korte, C., Kozur, H. W., Bruckschen, P., & Veizer, J. (2003). Strontium isotope evolution of
899 Late Permian and Triassic seawater. *Geochimica et Cosmochimica Acta, 67*(1), 47-62.
900 https://doi.org/10.1016/S0016-7037(02)01035-9
901 Korte, C., Ruhl, M., Pálfy, J., Ullmann, C. V., & Hesselbo, S. P. (2018). Chemostratigraphy
902 across the Triassic–Jurassic boundary. *Chemostratigraphy across major chronological*
903 *boundaries*, 183-210. https://doi.org/10.1002/9781119382508.ch10
904 Korte, C., & Ullmann, C. V. (2018). Permian strontium isotope stratigraphy. *Geological Society,*
905 *London, Special Publications, 450*(1), 105-118. https://doi.org/10.1144/SP450.5
906 Kovács, E. B., Ruhl, M., Demény, A., Fórizs, I., Hegyi, I., Horváth-Kostka, Z. R., et al. (2020).
907 Mercury anomalies and carbon isotope excursions in the western Tethyan Csővár section
908 support the link between CAMP volcanism and the end-Triassic extinction. *Global and*
909 *Planetary Change, 194*, 103291. https://doi.org/10.1016/j.gloplacha.2020.103291

910 Kovács, Z., Demangel, I., Richoz, S., Hippler, D., Baldermann, A., & Krystyn, L. (2020). New
911 constraints on the evolution of $^{87}Sr/^{86}Sr$ of seawater during the Upper Triassic. *Global*
912 *and Planetary Change, 192*, 103255. https://doi.org/10.1016/j.gloplacha.2020.103255
913 Kozur, H. (1991). New Middle Carnian and Rhaetian conodonts from Hungary and the Alps.
914 Stratigraphic importance and tectonic implications for the Buda Mountains and adjacent
915 areas. *Jahrbuch der Geologischen Bundesanstalt, 134*(2), 271-297.
916 Kozur, H. (1993). First evidence of Liassic in the vicinity of Csövár (Hungary), and its
917 Paleogeographic and Paleotectonic significance. *Jahrbuch der Geologischen*
918 *Bundesanstalt, 136*(1), 89-98.
919 Kuroda, J., Hori, R. S., Suzuki, K., Gröcke, D. R., & Ohkouchi, N. (2010). Marine osmium
920 isotope record across the Triassic-Jurassic boundary from a Pacific pelagic site. *Geology,*
921 *38*(12), 1095-1098. https://doi.org/10.1130/G31223.1
922 Li, D., Shields-Zhou, G. A., Ling, H.-F., & Thirlwall, M. (2011). Dissolution methods for
923 strontium isotope stratigraphy: Guidelines for the use of bulk carbonate and phosphorite
924 rocks. *Chemical Geology, 290*(3-4), 133-144.
925 https://doi.org/10.1016/j.chemgeo.2011.09.004
926 Li, G., & Elderfield, H. (2013). Evolution of carbon cycle over the past 100 million years.
927 *Geochimica et Cosmochimica Acta*, 103, 11-25.
928 https://doi.org/10.1016/j.gca.2012.10.014
929 Lindström, S., Sanei, H., Van De Schootbrugge, B., Pedersen, G. K., Lesher, C. E., Tegner, C., et
930 al. (2019). Volcanic mercury and mutagenesis in land plants during the end-Triassic mass
931 extinction. *Science Advances, 5*(10), eaaw4018. https://doi.org/10.1126/sciadv.aaw4018

Marshall, C. R. (2023). Forty years later: The status of the “Big Five” mass extinctions. *Cambridge Prisms: Extinction, 1*, e5. https://doi.org/10.1017/ext.2022.4.pr7

Marzoli, A., Callegaro, S., Dal Corso, J., Davies, J. H. F. L., Chiaradia, M., Youbi, N., et al. (2018). The Central Atlantic Magmatic Province (CAMP): A Review. In L. H. Tanner (Ed.), *The Late Triassic World: Earth in a Time of Transition* (pp. 91-125). Cham: Springer International Publishing. https://doi.org/10.1007/978-3-319-68009-5_4

McArthur, J. (1994). Recent trends in strontium isotope stratigraphy. *Terra Nova*, *6*(4), 331-358. https://doi.org/10.1111/j.1365-3121.1994.tb00507.x

McArthur, J. (2008). Comment on “The impact of the Central Atlantic Magmatic Province on climate and on the Sr-and Os-isotope evolution of seawater” by Cohen AS and Coe AL 2007, Palaeogeography, Palaeoclimatology, Palaeoecology 244, 374–390. *Palaeogeography, Palaeoclimatology, Palaeoecology*, *263*(3-4), 146-149. https://doi.org/10.1016/j.palaeo.2007.09.008

McArthur, J., Donovan, D., Thirlwall, M., Fouke, B., & Mattey, D. (2000). Strontium isotope profile of the early Toarcian (Jurassic) oceanic anoxic event, the duration of ammonite biozones, and belemnite palaeotemperatures. *Earth and Planetary Science Letters, 179*(2), 269-285. https://doi.org/10.1016/S0012-821X(00)00111-4

McArthur, J., Howarth, R., & Shields, G. (2012). Strontium isotope stratigraphy. In *Geologic Time Scale 2012* (pp. 127–144): Elsevier. https://doi.org/10.1016/B978-0-444-59425-9.00007-X

McArthur, J., Howarth, R., Shields, G., & Zhou, Y. (2020). Strontium isotope stratigraphy. In *Geologic Time Scale 2020* (pp. 211-238): Elsevier. https://doi.org/10.1016/B978-0-12-824360-2.00007-3

McElwain, J. C., Beerling, D. J., & Woodward, F. I. (1999). Fossil plants and global warming at the Triassic-Jurassic Boundary. *Science, 285*(5432), 1386-1390. https://doi.org/10.1126/science.285.5432.1386

McHone, J. G. (2000). Non-plume magmatism and rifting during the opening of the central Atlantic Ocean. *Tectonophysics, 316*, 287-296. https://doi.org/10.1016/S0040-1951(99)00260-7

Merle, R., Marzoli, A., Bertrand, H., Reisberg, L., Verati, C., Zimmermann, C., et al. (2011). $^{40}Ar/^{39}Ar$ ages and Sr–Nd–Pb–Os geochemistry of CAMP tholeiites from Western Maranhão basin (NE Brazil). *Lithos, 122*(3-4), 137-151. https://doi.org/10.1016/j.lithos.2010.12.010

Michalík, J., Lintnerová, O., Gaździcki, A., & Soták, J. (2007). Record of environmental changes in the Triassic–Jurassic boundary interval in the Zliechov Basin, Western Carpathians. *Palaeogeography, Palaeoclimatology, Palaeoecology, 244*(1-4), 71-88. https://doi.org/10.1016/j.palaeo.2006.06.024

Newton, R., Pevitt, E., Wignall, P., & Bottrell, S. (2004). Large shifts in the isotopic composition of seawater sulphate across the Permo–Triassic boundary in northern Italy. *Earth and Planetary Science Letters, 218*(3-4), 331-345. https://doi.org/10.1016/S0012-821X(03)00676-9

Onoue, T., Michalík, J., Shirozu, H., Yamashita, M., Yamashita, K., Kusaka, S., & Soda, K. (2022). Extreme continental weathering in the northwestern Tethys during the end-Triassic mass extinction. *Palaeogeography, Palaeoclimatology, Palaeoecology, 594*, 110934. https://doi.org/10.1016/j.palaeo.2022.110934

977 Onoue, T., Yamashita, K., Fukuda, C., Soda, K., Tomimatsu, Y., Abate, B., & Rigo, M. (2018).
978 Sr isotope variations in the Upper Triassic succession at Pizzo Mondello, Sicily:
979 Constraints on the timing of the Cimmerian Orogeny. *Palaeogeography,*
980 *Palaeoclimatology, Palaeoecology, 499*, 131-137.
981 https://doi.org/10.1016/j.palaeo.2018.03.025
982 Pálfy, J., Demény, A., Haas, J., Carter, E. S., Görög, Á., Halász, D., et al. (2007). Triassic–
983 Jurassic boundary events inferred from integrated stratigraphy of the Csővár section,
984 Hungary. *Palaeogeography, Palaeoclimatology, Palaeoecology*, *244*(1-4), 11-33.
985 https://doi.org/10.1016/j.palaeo.2006.06.021
986 Pálfy, J., Demény, A., Haas, J., Hetényi, M., Orchard, M. J., & Veto, I. (2001). Carbon isotope
987 anomaly and other geochemical changes at the Triassic-Jurassic boundary from a marine
988 section in Hungary. *Geology*, *29*(11), 1047-1050. https://doi.org/10.1130/0091-
989 7613(2001)029<1047:CIAAOG>2.0.CO;2
990 Pálfy, J., & Dosztály, L. (2000). A new marine Triassic-Jurassic boundary section in Hungary.
991 *GeoResearch Forum, 6*, 173-179.
992 Pálfy, J., & Kocsis, A. (2014). Volcanism of the Central Atlantic magmatic province as the
993 trigger of environmental and biotic changes around the Triassic–Jurassic boundary. In G.
994 Keller & A. C. Kerr (Eds.), *Volcanism, impacts, and mass extinctions: Causes and*
995 *effects, Geological Society of America Special Paper505*, 245-261.
996 https://doi.org/10.1130/2014.2505(12)
997 Pálfy, J., & Smith, P. L. (2000). Synchrony between Early Jurassic extinction, oceanic anoxic
998 event, and the Karoo-Ferrar flood basalt volcanism. *Geology*, *28*(8), 747-750.
999 https://doi.org/10.1130/0091-7613(2000)28<747:SBEJEO>2.0.CO;2

Palmer, M., & Edmond, J. (1989). The strontium isotope budget of the modern ocean. *Earth and Planetary Science Letters*, 92(1), 11-26. https://doi.org/10.1016/0012-821X(89)90017-4

Pearce, C. R., Parkinson, I. J., Gaillardet, J., Charlier, B. L., Mokadem, F., & Burton, K. W. (2015). Reassessing the stable (δ88/86Sr) and radiogenic (87Sr/86Sr) strontium isotopic composition of marine inputs. *Geochimica et Cosmochimica Acta*, *157*, 125-146. https://doi.org/10.1016/j.gca.2015.02.029

Percival, L. M., Ruhl, M., Hesselbo, S. P., Jenkyns, H. C., Mather, T. A., & Whiteside, J. H. (2017). Mercury evidence for pulsed volcanism during the end-Triassic mass extinction. *Proceedings of the National Academy of Sciences*, *114*(30), 7929-7934. https://doi.org/10.1073/pnas.1705378114

Peucker-Ehrenbrink, B., & Fiske, G. J. (2019). A continental perspective of the seawater $^{87}Sr/^{86}Sr$ record: a review. *Chemical Geology*, 510, 140-165. https://doi.org/10.1016/j.chemgeo.2019.01.017

Richter, F. M., & Turekian, K. K. (1993). Simple models for the geochemical response of the ocean to climatic and tectonic forcing. *Earth and Planetary Science Letters*, *119*(1-2), 121-131. https://doi.org/10.1016/0012-821X(93)90010-7

Rizzi, M., Thibault, N., Ullmann, C. V., Ruhl, M., Olsen, T. K., Moreau, J., et al. (2020). Sedimentology and carbon isotope stratigraphy of the Rhaetian Hochalm section (Late Triassic, Austria). *Global and Planetary Change*, 191, 103210. https://doi.org/10.1016/j.gloplacha.2020.103210

Ruhl, M., Deenen, M., Abels, H., Bonis, N., Krijgsman, W., & Kürschner, W. (2010). Astronomical constraints on the duration of the early Jurassic Hettangian stage and recovery rates following the end-Triassic mass extinction (St Audrie's Bay/East

Quantoxhead, UK). *Earth and Planetary Science Letters*, *295*(1-2), 262-276. https://doi.org/10.1016/j.epsl.2010.04.008

Ruhl, M., Hesselbo, S. P., Al-Suwaidi, A., Jenkyns, H., Damborenea, S. E., Manceñido, M. O., et al. (2020). On the onset of Central Atlantic Magmatic Province (CAMP) volcanism and environmental and carbon-cycle change at the Triassic–Jurassic transition (Neuquén Basin, Argentina). *Earth-Science Reviews*, *208*, 103229. https://doi.org/10.1016/j.earscirev.2020.103229

Ruhl, M., & Kürschner, W. (2011). Multiple phases of carbon cycle disturbance from large igneous province formation at the Triassic-Jurassic transition. *Geology*, *39*(5), 431-434. https://doi.org/10.1130/G31680.1

Saltzman, M. R., & Sedlacek, A. R. (2013). Chemostratigraphy indicates a relatively complete Late Permian to Early Triassic sequence in the western United States. *Geology*, *41*(4), 399-402. https://doi.org/10.1130/G33906.1

Schaller, M. F., Wright, J. D., & Kent, D. V. (2011). Atmospheric p CO2 perturbations associated with the Central Atlantic Magmatic Province. *Science*, *331*(6023), 1404-1409. https://doi.org/10.1126/science.1199011

Schaller, M. F., Wright, J. D., Kent, D. V., & Olsen, P. E. (2012). Rapid emplacement of the Central Atlantic Magmatic Province as a net sink for CO2. *Earth and Planetary Science Letters*, *323*, 27-39. https://doi.org/10.1016/j.epsl.2011.12.028

Sepkoski Jr, J. J. (1996). Patterns of Phanerozoic extinction: a perspective from global data bases. In *Global Events and Event Stratigraphy in the Phanerozoic: Results of the International Interdisciplinary Cooperation in the IGCP-Project 216 "Global Biological*

Events in Earth History" (pp. 35-51): Springer. https://doi.org/10.1007/978-3-642-79634-0_4

Shen, J., Yin, R., Algeo, T. J., Svensen, H. H., & Schoepfer, S. D. (2022a). Mercury evidence for combustion of organic-rich sediments during the end-Triassic crisis. *Nature Communications, 13*(1), 1307. https://doi.org/10.1038/s41467-022-28891-8

Shen, J., Yin, R., Zhang, S., Algeo, T. J., Bottjer, D. J., Yu, J., et al. (2022b). Intensified continental chemical weathering and carbon-cycle perturbations linked to volcanism during the Triassic–Jurassic transition. *Nature Communications*, *13*(1), 299. https://doi.org/10.1038/s41467-022-27965-x

Somlyay, A., Palcsu, L., Kiss, G. I., Clarkson, M. O., Kovács, E. B., Vallner, Z., et al. (2023). Uranium isotope evidence for extensive seafloor anoxia after the end-Triassic mass extinction. *Earth and Planetary Science Letters*, *614*, 118190. https://doi.org/10.1016/j.epsl.2023.118190

Song, H., Wignall, P. B., Tong, J., Song, H., Chen, J., Chu, D., et al. (2015). Integrated Sr isotope variations and global environmental changes through the Late Permian to early Late Triassic. *Earth and Planetary Science Letters*, *424*, 140-147. https://doi.org/10.1016/j.epsl.2015.05.035

Storm, M. S., Hesselbo, S. P., Jenkyns, H. C., Ruhl, M., Ullmann, C. V., Xu, W., et al. (2020). Orbital pacing and secular evolution of the Early Jurassic carbon cycle. *Proceedings of the National Academy of Sciences, 117*(8), 3974-3982. https://doi.org/10.1073/pnas.1912094117

Tackett, L. S., Kaufman, A. J., Corsetti, F. A., & Bottjer, D. J. (2014). Strontium isotope stratigraphy of the Gabbs Formation (Nevada): implications for global Norian–Rhaetian

correlations and faunal turnover. *Lethaia*, *47*(4), 500-511. https://doi.org/10.1111/let.12075

Thibodeau, A. M., Ritterbush, K., Yager, J. A., West, A. J., Ibarra, Y., Bottjer, D. J., et al. (2016). Mercury anomalies and the timing of biotic recovery following the end-Triassic mass extinction. *Nature Communications*, *7*(1), 11147. https://doi.org/10.1038/ncomms11147

Vallner, Z., Kovács, E. B., Haas, J., Móricz, F., Ruhl, M., Zajzon, N., & Pálfy, J. (2023). Preservation of orbital forcing in intraplatform carbonates and an astronomical time frame for a multiproxy record of end-Triassic global change from a western Tethyan section (Csővár, Hungary). *Palaeogeography, Palaeoclimatology, Palaeoecology*, 111493. https://doi.org/10.1016/j.palaeo.2023.111493

van de Schootbrugge, B., van Der Weijst, C., Hollaar, T., Vecoli, M., Strother, P., Kuhlmann, N., et al. (2020). Catastrophic soil loss associated with end-Triassic deforestation. *Earth-Science Reviews*, *210*, 103332. https://doi.org/10.1016/j.earscirev.2020.103332

van de Schootbrugge, B. A. S., & Wignall, P. B. (2015). A tale of two extinctions: converging end-Permian and end-Triassic scenarios. *Geological Magazine*, *153*(2), 332-354. https://doi.org/10.1017/S0016756815000643

Veizer, J., & Compston, W. (1974). 87Sr/86Sr composition of seawater during the Phanerozoic. *Geochimica et Cosmochimica Acta*, *38*(9), 1461-1484. https://doi.org/10.1016/0016-7037(74)90099-4

Ward, P., Haggart, J., Carter, E., Wilbur, D., Tipper, H., & Evans, T. (2001). Sudden productivity collapse associated with the Triassic-Jurassic boundary mass extinction. *Science*, *292*(5519), 1148-1151. https://doi.org/10.1126/science.1058574

Weedon, G. P., Jenkyns, H. C., & Page, K. N. (2018). Combined sea-level and climate controls on limestone formation, hiatuses and ammonite preservation in the Blue Lias Formation, South Britain (uppermost Triassic–Lower Jurassic). *Geological Magazine, 155*(5), 1117-1149. https://doi.org/10.1017/S001675681600128X

Weedon, G. P., Page, K. N., & Jenkyns, H. C. (2019). Cyclostratigraphy, stratigraphic gaps and the duration of the Hettangian Stage (Jurassic): insights from the Blue Lias Formation of southern Britain. *Geological Magazine, 156*(9), 1469-1509. https://doi.org/10.1017/S0016756818000808

Wignall, P. (2005). The link between large igneous province eruptions and mass extinctions. *Elements, 1*(5), 293-297. https://doi.org/10.2113/gselements.1.5.293

Wotzlaw, J.-F., Guex, J., Bartolini, A., Gallet, Y., Krystyn, L., McRoberts, C. A., et al. (2014). Towards accurate numerical calibration of the Late Triassic: High-precision U-Pb geochronology constraints on the duration of the Rhaetian. *Geology, 42*(7), 571-574. https://doi.org/10.1130/G35612.1

Yager, J. A., West, A. J., Thibodeau, A. M., Corsetti, F. A., Rigo, M., Berelson, W. M., et al. (2021). Mercury contents and isotope ratios from diverse depositional environments across the Triassic–Jurassic Boundary: Towards a more robust mercury proxy for large igneous province magmatism. *Earth-Science Reviews, 223*, 103775. https://doi.org/10.1016/j.earscirev.2021.103775

Yobo, L. N., Brandon, A. D., Holmden, C., Lau, K. V., & Eldrett, J. (2021). Changing inputs of continental and submarine weathering sources of Sr to the oceans during OAE 2. *Geochimica et Cosmochimica Acta, 303*, 205-222. https://doi.org/10.1016/j.gca.2021.03.013

Zajzon, N., Kristály, F., Pálfy, J., & Németh, T. (2012). Detailed clay mineralogy of the Triassic-Jurassic boundary section at Kendlbachgraben (Northern Calcareous Alps, Austria). *Clay Minerals*, *47*, 177-189. https://doi.org/10.1180/claymin.2012.047.2.03

Zhou, Y., Pogge von Strandmann, P. A., Zhu, M., Ling, H., Manning, C., Li, D., et al. (2020). Reconstructing Tonian seawater $^{87}Sr/^{86}Sr$ using calcite microspar. *Geology*, *48*(5), 462-467. https://doi.org/10.1130/G46756.1